II. Institute of Physics

University of Cologne

Construction of a Polarization Spectrometer and Observation of the Skyrmion Phase in the Magneto-Electric Insulator Cu_2OSeO_3

Master Thesis

Supervised by Prof. Dr. Paul H. M. van Loosdrecht

Second Referee Prof. Dr. Achim Rosch

Submitted by Simon Schäfer

Matriculation Number 5018587

May 9, 2015

Cologne 2014/2015

Contents

1. Introduction

1.1. Motivation

In the late 19th century, Michael Faraday and John Kerr discovered two effects that started the field of magneto-optics. Faraday observed that the polarization of light transmitted through magnetized materials is changed, Kerr found the same to be true a few years later for light reflected from magnetic samples. The effects are today termed Faraday effect and magneto-optical Kerr effect (MOKE, pictured in figure 1.1) after their discoverers and both are caused by a magnetization of the sample – either through an applied external field or through remnant magnetic order, for example in ferromagnets. To first order, the sizes of both Faraday

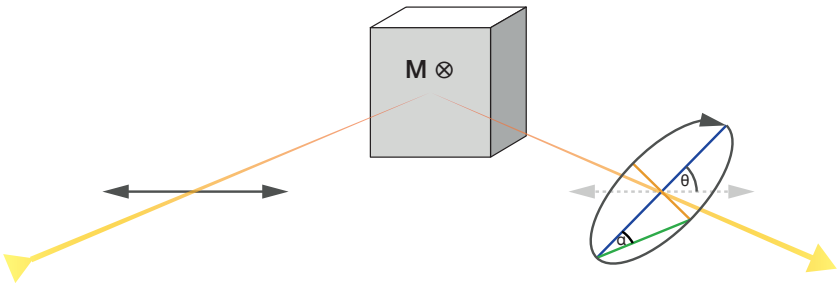

Figure 1.1.: An illustration of the magneto-optical Kerr effect. Linearly polarized light is reflected from a sample with magnetization M and its polarization state is changed: After reflection, the polarization is elliptical with rotation angle θ and ellipticity angle α.

effect and MOKE are proportional to the magnetization of the sample[1], which is why they can be used as an effective optical probe for magnetization behavior. The main advantages in comparison to other techniques like SQUID are the possibility of quick in-situ measurements and spatial resolution using MOKE microscopy. In a SQUID setup, the averaged magnetization of the whole sample is determined; with a MOKE microscope one can resolve spatial features like magnetic domains, the upper resolution bound being the Abbe diffraction limit of the employed system. Also for very small samples or thin films, MOKE measurements can give good results.

The high spatial resolution led to the introduction of magneto-optical (MO) storage media

in the 1980s[2], with widespread commercial success in the 1990s. In one such medium, the MiniDisc, the data is recorded magnetically and read out with a laser using magneto-optical effects. While these storage solutions have today have mostly lost their relevance, MO effects continue to play an important role in science. They can give insights into the internal structure and also, with their time-resolved analysis on the femtosecond scale, dynamics of materials.

During the course of this thesis, a polarization spectrometer was built. It can be used to measure MO effects in both reflection and transmission geometries and features a superconducting magnet with a built-in cryostat. The direction of the magnetic field is parallel to the incoming light, which in terms of MOKE is called the "polar" Kerr effect (see figure 1.2). Cu_2OSeO_3 was chosen as the first material to be investigated. It is an insulator that is

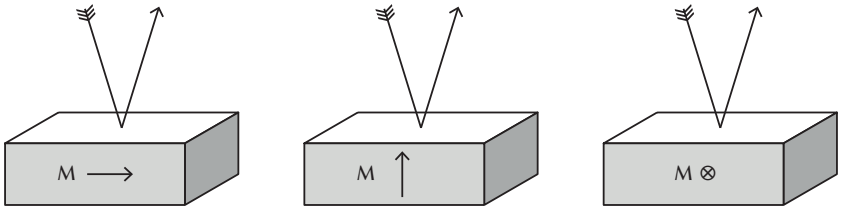

Figure 1.2.: Three different MOKE geometries depending on the orientation of the incoming light and the magnetization direction of the sample: Longitudinal, polar and transverse. The polar configuration is often chosen as it causes the largest change in polarization[3].

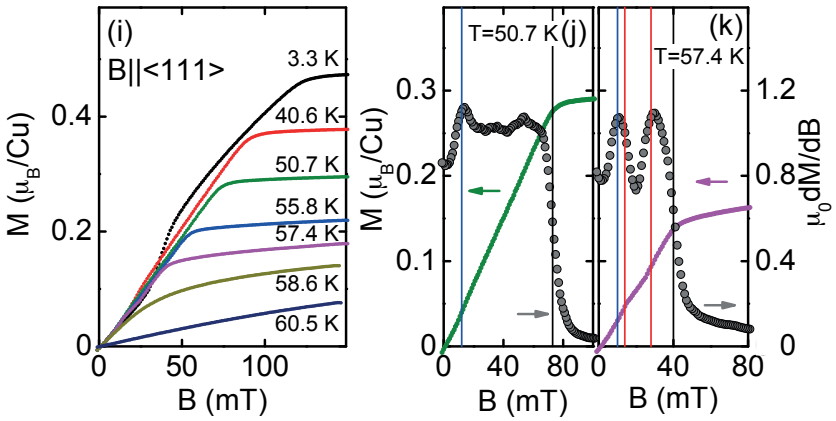

Figure 1.3.: SQUID data from a publication by Adams et al.[4]. Given on the left are the magnetization curves of the Cu_2OSeO_3 sample for different temperatures. In the first derivative of the magnetization data, given on the right for two temperatures, they find a distinct dip depending on whether the sample is in the skyrmion phase (k) or not (j).

the object of much current research because it hosts a skyrmion phase (for more details see section 3.1). The reasons for doing magneto-optical spectroscopy on this compound were

twofold: Firstly, we wanted to find out whether the skyrmion lattice has a special effect on the polarization state of the reflected light. Secondly, because the MOKE signal is approximately proportional to the magnetization of the material, we expected to replicate the kinks in the magnetization behavior around the skyrmion phase as found by Adams et al. in SQUID measurements (see figure 1.3).

1.2. Fundamentals

Polarized Light

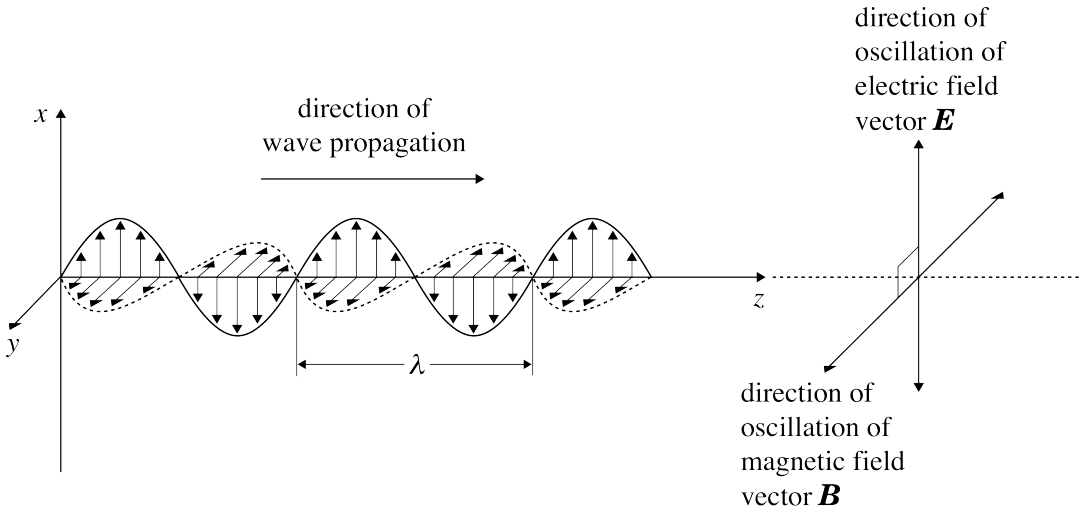

Figure 1.4.: Illustration of a linearly polarized wave. **E** and **B** field vectors are perpendicular and stay within the same planes parallel to the propagation vector at all times. Image from [5].

Light traveling in free space is a transverse electromagnetic wave with electric and magnetic fields perpendicular to each other, such that $\mathbf{E} \times \mathbf{B}$ points in the wave's propagation direction. As such, it can be *polarized*: If the electric field vector oscillates in a fixed direction in space that does not change in time, the light is linearly polarized (see figure 1.4). If the oscillation direction is not constant in time, the electric field vector traces out an ellipse and the light is elliptically polarized. In figure 1.5b, θ is the angle between the ellipse's major axis (in blue) and the x-axis. The ratio of the minor and major axes is called ellipticity, $\epsilon = \frac{l_{\text{minor}}}{l_{\text{major}}}$, often expressed with an angle such that $\tan\alpha = \epsilon$.
The special case $\epsilon = 1$ leads to circular polarization. This is depicted in figure 1.5a and further explained in the next section.

Jones Calculus

In 1941, R. C. Jones proposed[6] an elegant formalism for the description of fully polarized (monochromatic) light that employs vectors to describe the polarization state and matrices to describe polarizing elements. For a light ray propagating in the z-direction, the electric field vector lies in the x-y plane. Its time-dependent oscillation can be described by:

$$\begin{aligned}\mathbf{E}(t) = \begin{pmatrix} E_x(t) \\ E_y(t) \end{pmatrix} &= \begin{pmatrix} E_{0x} e^{i(kz-\omega t)} \\ E_{0y} e^{i(kz-\omega t+\phi)} \end{pmatrix} \\ &= \underbrace{\begin{pmatrix} E_{0x} \\ E_{0y} e^{i\phi} \end{pmatrix}}_{\mathbf{J}} e^{i(kz-\omega t)} \end{aligned} \tag{1.1}$$

The vector **J** is called the *Jones vector*. The phase difference ϕ makes the polarization elliptical as it shifts the x and y components with respect to each other (see figure 1.5a).
The special case with $E_{0x} = E_{0y}$ and a phase difference ϕ of $\pm\frac{\pi}{2}$ is called circularly polarized light. The definition of left (LCP) and right (RCP) circular polarization is a source of lasting confusion. There exist two different viewpoints: One is describing the rotation from the point of the *receiver*. In this case, the electric field vector of figure 1.5a will rotate clockwise (right-handed) in time. The other, also often used convention looks at the wave from the point of the *source*. From there, the electric field vector will seem to rotate counterclockwise (left-handed). In this thesis, we will look at the light beam from the position of the receiver. This gives us the following definitions:

$$\text{RCP} : \mathbf{e}_- = \frac{1}{\sqrt{2}} \begin{pmatrix} 1 \\ -i \end{pmatrix}, \qquad \text{LCP} : \mathbf{e}_+ = \frac{1}{\sqrt{2}} \begin{pmatrix} 1 \\ i \end{pmatrix} \tag{1.2}$$

Note that a combination of RCP and LCP light with equal amplitudes is again a linearly polarized wave.

Bases

While the Cartesian representation with basis vectors $\hat{\mathbf{x}} = \left(\begin{smallmatrix} 1 \\ 0 \end{smallmatrix}\right)$ and $\hat{\mathbf{y}} = \left(\begin{smallmatrix} 0 \\ 1 \end{smallmatrix}\right)$ may be the most intuitive way to span the polarization vector space, any set of orthogonal vectors can also be used.
It is often convenient to use the circular polarization states $\mathbf{e}_-$ and $\mathbf{e}_+$ as a basis. For example,

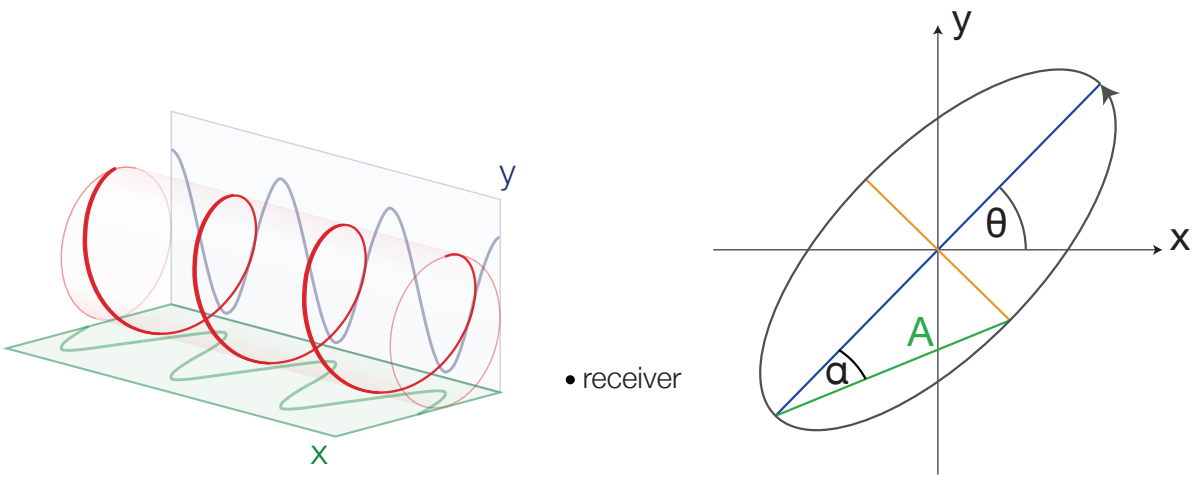

(a) Illustration of how two sine waves with a phase difference overlay to create an elliptical wave. Depicted is the special case $\Delta\phi = \frac{\pi}{2}$ which results in circularly polarized light. Image created with parts from [7].

(b) An ellipse is the most general polarization state. Parameters are the rotation of its major axis and the ratio of the two axes.

Figure 1.5.: Circular and elliptical polarization

in media with a broken time-reversal symmetry due to a magnetic field, the eigenmodes of light propagation in the material are circular modes. The transformation matrices to go from Cartesian to circular representation and its inverse are:

$$F = \frac{1}{\sqrt{2}} \begin{pmatrix} 1 & i \\ 1 & -i \end{pmatrix}, \quad F^{-1} = \frac{1}{\sqrt{2}} \begin{pmatrix} 1 & 1 \\ -i & i \end{pmatrix} \tag{1.3}$$

The Cartesian basis vectors are written in a circular basis as follows:

$$[\hat{\mathbf{x}}]_{\pm} = F \cdot \begin{pmatrix} 1 \\ 0 \end{pmatrix} = \frac{1}{\sqrt{2}} \begin{pmatrix} 1 \\ 1 \end{pmatrix}, \qquad [\hat{\mathbf{y}}]_{\pm} = F \cdot \begin{pmatrix} 0 \\ 1 \end{pmatrix} = \frac{i}{\sqrt{2}} \begin{pmatrix} 1 \\ -1 \end{pmatrix} \tag{1.4}$$

This will be useful in later chapters.

Elliptical Light

The generalization of circular to elliptical light is straightforward[8]. Using figure 1.5b as a reference, we start with a circularly polarized (here: $\mathbf{e}_+$) Jones vector and scale the x and y components with $A\cos\alpha$ and $A\sin\alpha$, respectively, to get the desired ratio between the

major/minor axis:

$$\mathbf{E}' = \frac{1}{\sqrt{2}} \begin{pmatrix} A\cos\alpha \\ iA\sin\alpha \end{pmatrix} \tag{1.5}$$

The rotation of the ellipse is then achieved by multiplying with a rotation matrix $R(\theta) = \left(\begin{smallmatrix} \cos\theta & -\sin\theta \\ \sin\theta & \cos\theta \end{smallmatrix}\right)$:

$$\mathbf{E}'' = R(\theta)\mathbf{E}' \tag{1.6}$$

We decompose this vector into circular components using the transformation matrix from the previous section:

$$\begin{pmatrix} E_- \\ E_+ \end{pmatrix} = F \cdot \mathbf{E}'' = \frac{A}{\sqrt{2}} \begin{pmatrix} e^{i\theta}(\cos\alpha - \sin\alpha) \\ e^{-i\theta}(\cos\alpha + \sin\alpha) \end{pmatrix} \tag{1.7}$$

Along the lines of [8], we define a polarization variable ζ as the ratio of the two components:

$$\zeta := \frac{E_+}{E_-} = e^{-2i\theta}\frac{1+\tan\alpha}{1-\tan\alpha} = e^{-2i\theta}\frac{1+\epsilon}{1-\epsilon} \tag{1.8}$$

This allows us to express rotation and ellipticity of the ellipse as functions of this ratio:

$$\theta = -\frac{1}{2}\arg\zeta, \qquad \epsilon = \frac{|\zeta|-1}{|\zeta|+1} \tag{1.9}$$

Optical Elements

In Jones calculus, linear optical elements are described by 2×2-matrices. They are applied to the Jones vector to receive the corresponding new polarization states. In the case that there are several optical elements, their respective matrices are multiplied with the Jones vector in the direction that the light passes them:

$$\mathbf{E}_{\text{final}} = M_n \cdot M_{n-1} \cdot \ldots \cdot M_2 \cdot M_1 \cdot \mathbf{E}_{\text{initial}} \tag{1.10}$$

As an example: It is intuitively clear that (ideal) polarizers P_x and P_y that let only light polarized in the x/y-direction pass through should have the following matrix representations:

$$P_x \cdot \begin{pmatrix} E_x(t) \\ E_y(t) \end{pmatrix} \stackrel{!}{=} \begin{pmatrix} E_x(t) \\ 0 \end{pmatrix}$$
$$\curvearrowright P_x = \begin{pmatrix} 1 & 0 \\ 0 & 0 \end{pmatrix}$$
$$P_y \cdot \begin{pmatrix} E_x(t) \\ E_y(t) \end{pmatrix} \stackrel{!}{=} \begin{pmatrix} 0 \\ E_y(t) \end{pmatrix}$$
$$\curvearrowright P_y = \begin{pmatrix} 0 & 0 \\ 0 & 1 \end{pmatrix}$$

Also, their product $P_x \cdot P_y$ is the zero matrix, which replicates the behavior that crossed polarizers block light.
The expression for a polarizer at an arbitrary angle and some other optical elements can be found in table A.1 in the appendix.

Lorentz Oscillator in a Magnetic Field

The magneto-optical Kerr effect has its origins in quantum effects such as spin-orbit coupling and exchange interaction[9]. Nevertheless, we can provide a classical example (adapted from [10]) that illustrates how an external magnetic field can cause Kerr and Faraday effects: We will calculate the Lorentz oscillator model within an external magnetic field. In this model, the electron (or the electron "cloud") with mass m is connected to the infinitely heavy nucleus via a spring force. There is also a damping term, as the moving electron is expected to lose energy by emitting radiation. An external electric field, like that of an electromagnetic wave, is the driving force. The external magnetic field (this may also be an internal magnetization) acts on the moving electron via the Lorentz force. The equation of motion is:

$$\ddot{\mathbf{r}} + \gamma\dot{\mathbf{r}} + \omega_0^2\mathbf{r} = -\frac{e}{m}(\mathbf{E} + \dot{\mathbf{r}} \times \mathbf{B}) \tag{1.11}$$

Let the B field be in the z-direction, $\mathbf{B} = (0\ 0\ B)^\mathsf{T}$, as well as the propagation vector of the incoming light. This implies that the E-field of the light oscillates in the x-y plane: $\mathbf{E}(t) = (E_x(t)\ E_y(t)\ 0)^\mathsf{T} = e^{-i\omega t}(E_{x0}\ E_{y0}\ 0)^\mathsf{T}$. Using the ansatz $\mathbf{r} = \mathbf{r_0}e^{-i\omega t}$ we find:

$$(\omega_0 - i\gamma\omega - \omega^2)z_0 = 0 \tag{1.12}$$

This is the equation for a damped harmonic oscillator without a driving force, i.e. in the z-direction neither the electric nor the magnetic field are felt by the electron. We will thus ignore the z coordinate from now on.
For x and y we get a set of coupled equations:

$$\begin{pmatrix} A & -i\omega\omega_c \\ i\omega\omega_c & A \end{pmatrix} \begin{pmatrix} x_0 \\ y_0 \end{pmatrix} = -\frac{e}{m} \begin{pmatrix} E_{x0} \\ E_{y0} \end{pmatrix} \tag{1.13}$$

With $\omega_c = \frac{eB}{m}$ and $A = \omega_0 - i\gamma\omega - \omega^2$. The matrix in question can be diagonalized by transforming the system to a circular basis. We define:

$$r_0^+ := x_0 + iy_0, \quad r_0^- := x_0 - iy_0 \tag{1.14}$$

$$E_0^+ := E_{x0} + iE_{y0}, \quad E_0^- := E_{x0} - iE_{y0} \tag{1.15}$$

Along with this, we use the transformation matrices from equation 1.3 to go from Cartesian to circular representation. Applying this to equation 1.13, we receive a solution in terms of the new variables:

$$F \begin{pmatrix} A & -i\omega\omega_c \\ i\omega\omega_c & A \end{pmatrix} F^{-1} \begin{pmatrix} r_0^+ \\ r_0^- \end{pmatrix} = \begin{pmatrix} A - \omega\omega_c & 0 \\ 0 & A + \omega\omega_c \end{pmatrix} \begin{pmatrix} r_0^+ \\ r_0^- \end{pmatrix} = -\frac{e}{m} \begin{pmatrix} E_0^+ \\ E_0^- \end{pmatrix}$$

$$\curvearrowright r_0^+ = -\frac{eE_0^+}{m(A - \omega\omega_c)}, \qquad r_0^- = -\frac{eE_0^-}{m(A + \omega\omega_c)} \tag{1.16}$$

From this, we can calculate the macroscopic polarization (for N electrons), the susceptibility and the dielectric function:

$$P^\pm = Nqr^\pm(t) \curvearrowright \chi^\pm = \frac{P^\pm}{\varepsilon_0 E^\pm} = \frac{Ner^\pm}{E^\pm} \curvearrowright \varepsilon^\pm = 1 + \frac{Ner^\pm}{E^\pm}$$

$$\varepsilon^\pm = -\frac{Ne^2}{m(A \mp \omega\omega_c)} \tag{1.17}$$

We have found the dielectric function with different elements for right and left circularly polarized light. It can be written as a matrix $\varepsilon_{\text{circ}} = \begin{pmatrix} \varepsilon^+ & 0 \\ 0 & \varepsilon^- \end{pmatrix}$. This implies that there are two refractive indices $n_\pm = \sqrt{\varepsilon_\pm}$ for RCP and LCP light, respectively. Although the underlying theory is much more complex in reality, this is an illustrative example of the dielectric tensor properties that cause Faraday and Kerr effects in the material.
If we perform the transformation back to Cartesian coordinates, we find that in this basis

there are antisymmetric off-diagonal terms that we will discuss in the next sections:

$$\varepsilon_{\text{Cart}} = F^{-1}\varepsilon_{\text{circ}}F = \begin{pmatrix} \varepsilon^+ + \varepsilon^- & i(\varepsilon^+ - \varepsilon^-) \\ -i(\varepsilon^+ - \varepsilon^-) & \varepsilon^+ + \varepsilon^- \end{pmatrix} \tag{1.18}$$

Connection between measured quantities and reflective properties

We now want to derive a relation between the measurable Kerr angle θ_k and ellipticity ϵ_k on one hand and the dielectric tensor on the other hand.
Although we will not achieve perfect normal incidence because of limitations in our measurement setup (see section 2), the expected angle between incoming and reflected beam is small enough to treat it as such. The Fresnel formula for reflection at normal incidence is[11]:

$$\tilde{\rho}(\omega) = \frac{\tilde{n}(\omega) - 1}{\tilde{n}(\omega) + 1} \tag{1.19}$$

Here, $\tilde{n}(\omega)$ denotes the complex refractive index which is closely related to the dielectric function/tensor:

$$\tilde{n} = \sqrt{\tilde{\varepsilon}} = n + ik \tag{1.20}$$

We will drop the notation of the ω-dependence from now on.
The complex reflection coefficient $\tilde{\rho}$ describes the ratio in intensity between incident and reflected light, as well as a phase difference θ introduced in the reflection process. As we have established in the previous section, we expect a difference in reflection for right and left circularly polarized light:

$$\tilde{\rho}_\pm = r_\pm e^{i\theta_\pm} = \frac{\tilde{n}_\pm - 1}{\tilde{n}_\pm + 1} = \frac{\sqrt{\tilde{\varepsilon}_\pm} - 1}{\sqrt{\tilde{\varepsilon}_\pm} + 1} \tag{1.21}$$

In our particular measurement geometry, the incoming light $\mathbf{E}_{\text{in}}$ is linearly polarized; the outgoing beam $\mathbf{E}_{\text{out}}$ will in general have an elliptical polarization. Its polarization in terms of ζ as defined in section 1.2 will be:

$$\zeta_{\text{out}} = \frac{E_{\text{out},+}}{E_{\text{out},-}} = \frac{E_{\text{in},+}\tilde{\rho}_+}{E_{\text{in},-}\tilde{\rho}_-} = \frac{\tilde{\rho}_+}{\tilde{\rho}_-} \tag{1.22}$$

$$\curvearrowright \zeta_{\text{out}} = \frac{r_+}{r_-} e^{i(\theta_+ - \theta_-)} \tag{1.23}$$

The change in polarization and ellipticity as introduced by the Kerr-active sample is then quantified as (compare to equation 1.9):

$$\theta_k = -\frac{1}{2}(\theta_+ - \theta_-), \qquad \epsilon_k = \frac{\frac{r_+}{r_-} - 1}{\frac{r_+}{r_-} + 1} = \frac{r_+ - r_-}{r_+ + r_-} \tag{1.24}$$

Note that both $r_\pm$ and $\theta_\pm$ are frequency-dependent and that this is only valid for the polar geometry.

The Dielectric Tensor and Origins of MOKE

Under the influence of external electric fields (including light), charges in a material are displaced and the material becomes polarized. Excluding higher order responses, there will be a linear dependence between $\mathbf{E}$ and said polarization:

$$\mathbf{P} = \chi\varepsilon_0\mathbf{E}, \qquad \mathbf{D} = \varepsilon_0\mathbf{E} + \mathbf{P} = \varepsilon_0(1 + \chi)\mathbf{E}, \qquad \varepsilon = 1 + \chi \tag{1.25}$$

In anisotropic media, such as solid crystals, the response of the medium is in general not aligned with the direction of the external field. This means that in equation 1.25, the susceptibility χ is not a scalar, but a tensor. The quantity $\varepsilon = \mathbb{1} + \chi$ is called the *dielectric tensor*.

$$\varepsilon = \begin{pmatrix} \varepsilon_{xx} & \varepsilon_{xy} & \varepsilon_{xz} \\ \varepsilon_{yx} & \varepsilon_{yy} & \varepsilon_{yz} \\ \varepsilon_{zx} & \varepsilon_{zy} & \varepsilon_{zz} \end{pmatrix} = \mathbb{1} + \begin{pmatrix} \chi_{xx} & \chi_{xy} & \chi_{xz} \\ \chi_{yx} & \chi_{yy} & \chi_{yz} \\ \chi_{zx} & \chi_{zy} & \chi_{zz} \end{pmatrix} \tag{1.26}$$

In the simplified case of no external magnetic field, no absorption and no optical activity, the susceptibility tensor can be diagonalized along a set of principal axes. We then end up with a symmetric tensor whose off-diagonal elements are zero.
In the simplest cases of an isotropic (cubic) and a uniaxial (trigonal/tetragonal/hexagonal)

crystal, the dielectric tensor is simplified to:

$$\varepsilon_{\text{cubic}} = \begin{pmatrix} a & 0 & 0 \\ 0 & a & 0 \\ 0 & 0 & a \end{pmatrix}, \qquad \varepsilon_{xx} = \varepsilon_{yy} = \varepsilon_{zz} = a, \qquad n = \sqrt{a}$$

$$\varepsilon_{\text{uniaxial}} = \begin{pmatrix} a & 0 & 0 \\ 0 & a & 0 \\ 0 & 0 & b \end{pmatrix}, \qquad \varepsilon_{xx} = \varepsilon_{yy} = a, \varepsilon_{zz} = b, \qquad \begin{aligned} n_O &= \sqrt{a} \\ n_E &= \sqrt{b} \end{aligned} \tag{1.27}$$

In the cubic material, there is only one refractive index, n. The existence of two refractive indices in the uniaxial material is the source of linear birefringence, i.e. two beams with different linear polarizations get refracted differently.
The terms responsible for MOKE and the Faraday effect can be found on the off-diagonals of the dielectric tensor. These terms arise when time-reversal symmetry is broken in the material[1], for example as a consequence of an external magnetic field as shown with the Lorentz oscillator model. The effect of these elements on the Kerr and Faraday rotation will be quantified in the next section.

Dielectric Tensor and Optical Effects

Starting with a dielectric tensor for a cubic material with off-diagonal elements, we can calculate the Kerr and Faraday angles that will be measured in the material, following the lines of [8] and [12].

$$\varepsilon = \begin{pmatrix} \varepsilon_{xx} & \varepsilon_{xy} & 0 \\ -\varepsilon_{xy} & \varepsilon_{xx} & 0 \\ 0 & 0 & \varepsilon_{xx} \end{pmatrix} \tag{1.28}$$

We can diagonalize it by switching to a circular basis:

$$\varepsilon_{\text{circ}} = F\varepsilon F^{-1} = \begin{pmatrix} \varepsilon_{xx} - i\varepsilon_{xy} & 0 & 0 \\ 0 & \varepsilon_{xx} + i\varepsilon_{xy} & 0 \\ 0 & 0 & \varepsilon_{xx} \end{pmatrix} \tag{1.29}$$

For incident light along the z-axis, we can calculate the reflection with eq. 1.19:

$$\tilde{n}_{\pm} = \sqrt{\varepsilon_{xx} \pm i\varepsilon_{xy}} \tag{1.30}$$

$$\curvearrowright \tilde{\rho}_{\pm} = \frac{\tilde{n}_{\pm} - 1}{\tilde{n}_{\pm} + 1} \tag{1.31}$$

Using the definition of the polarization variable ζ from eq. 1.22, we receive:

$$\zeta = \frac{\tilde{\rho}_{+}}{\tilde{\rho}_{-}} \tag{1.32}$$

$$= 2 \cdot \frac{\sqrt{1 + i\frac{\varepsilon_{xy}}{\varepsilon_{xx}}} - \sqrt{1 - i\frac{\varepsilon_{xy}}{\varepsilon_{xx}}}}{\sqrt{\varepsilon_{xx} + \frac{\varepsilon_{xy}^2}{\varepsilon_{xx}}} - \sqrt{1 + i\frac{\varepsilon_{xy}}{\varepsilon_{xx}}} + \sqrt{1 - i\frac{\varepsilon_{xy}}{\varepsilon_{xx}}} - \frac{1}{\sqrt{\varepsilon_{xx}}}} + 1 \tag{1.33}$$

If we assume that ε_{xy} is small compared to ε_{xx}, we can use the approximation $\sqrt{1+x} \approx 1 + \frac{x}{2}$:

$$\zeta \approx \frac{2i\varepsilon_{xy}}{\sqrt{\varepsilon_{xx}}(\varepsilon_{xx} - 1) - i\varepsilon_{xy}} + 1 \tag{1.34}$$

$$\approx \frac{2i\varepsilon_{xy}}{\sqrt{\varepsilon_{xx}}(\varepsilon_{xx} - 1)} + 1 \tag{1.35}$$

We make one more approximation to eq. 1.8, assuming θ_k and ϵ_k to be small:

$$\zeta = e^{-2i\theta_k}\frac{1 + \epsilon_k}{1 - \epsilon_k} \approx (1 - 2i\theta_k) \cdot (1 + 2\epsilon_k) \tag{1.36}$$

$$\approx 1 - 2i\theta_k + 2\epsilon_k$$

Equating 1.36 and 1.34, we find:

$$\theta_k + i\epsilon_k = \frac{-\varepsilon_{xy}}{\sqrt{\varepsilon_{xx}}(\varepsilon_{xx} - 1)} \tag{1.37}$$

This connects the Kerr angles to the dielectric tensor.
For the Faraday effect, a similar expression can be calculated:

$$\theta_f + i\epsilon_f = \frac{\omega d}{2c}\frac{i\varepsilon_{xy}}{\sqrt{\varepsilon_{xx}}} \tag{1.38}$$

Here, ω is the frequency of the transmitted light and d is the traversed length of the material. Normal incidence is assumed. The full derivation can be found in [12].

2. Polarization Spectrometer Setup

2.1. Schematic

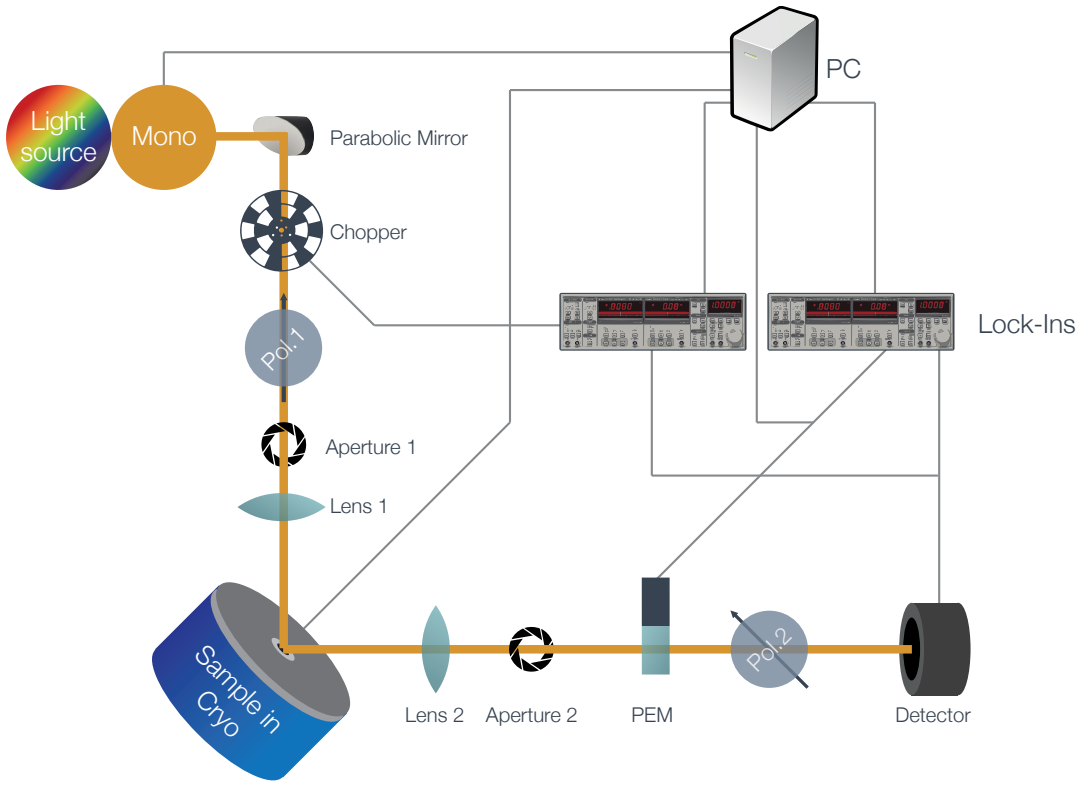

Figure 2.1.: Schematic of the setup — the MOKE configuration is depicted. The angle between incident and reflected light on the sample is exaggerated here for more visual clarity.

Broadband white light (~250nm up to near IR) is created by a xenon light source, the desired wavelength is then singled out via a computer-controlled Jobin Yvon MicroHR monochromator with adjustable gratings and color filters. The monochromator has an entrance and an exit slit that allow for an adjustable spectral width of the monochromated light. The light is collected and roughly collimated with an off-axis parabolic mirror, almost fully s-polarized by a Glan-Taylor prism and subsequently chopped with a frequency of ~600Hz. The chopper frequency serves as the reference for our first lock-in amplifier, which will yield us the DC intensity of the detected light.

The light is focused with a biconvex lens ($f = 15$cm) and impinges on the sample in the cryostat at almost normal (with an angle of ~7.5° to the surface normal) incidence with a spot size of around 1mm^2. The reflected light is refocused by a second $f = 15$cm lens and passes a photo-elastic modulator (PEM, described in section 2.2) and a second Glan-Taylor prism set at an angle of 135°. The PEM modulation frequency of 50kHz (and its second harmonic, see section 2.2) is the reference for the second lock-in amplifier. The light is detected by a silicon photodiode with an integrated amplifier; the signal is subsequently passed on to both lock-ins.

The original plans featured an off-axis parabolic mirror as a focusing device, as it is achromatic and should deliver the same spot size over the whole wavelength range. For reasons discussed in the appendix A.1, it changes the polarization of the incident light and cannot be used in the positions of the lenses as they are given in figure 2.1. Polarizing the light *after* focusing would be an option, but for the Glan-Taylor prisms to achieve good extinction ratios, the incoming light has to be as collimated as possible. Using a different kind of polarizer, e.g. sheet polarizers would mitigate the problem, but these cannot deliver the performance of Glan-Taylor prisms.

The measurement process has been mostly automated with the help of two custem LabVIEW programs. Screenshots and a description of the software can be found in the appendix A.4.

2.2. Photoelastic Modulator and the Polarization Modulation Technique

The polarization modulation technique as described by Sato[13] and others[8][12] improves on former techniques that involve manual rotation of polarizers or Faraday rotators. The central component of the setup is the photo-elastic modulator (PEM): It contains a piezoelectric element that introduces vibrations in the kHz range into a bar of transparent material (fused silica, in our case) that exhibits stress birefringence. The vibration frequency is tuned with respect to the speed of sound and the length of the bar, such that a standing wave with a maximum at the center is formed.

Light passing through the PEM will experience a periodic phase retardation due to stress birefringence — in so far as a polarization component is parallel to the optical axis of the PEM, typically the horizontal axis. The amplitude of retardation can be set on the PEM controller. In the special case of a 45° linearly polarized incoming wave and a retardation amplitude of $\lambda/2$, the modulated retardation will lead to a continuous variation between ±45° linearly and left-/right-circularly polarized states (see figure 2.2). In combination with two linear polariz-

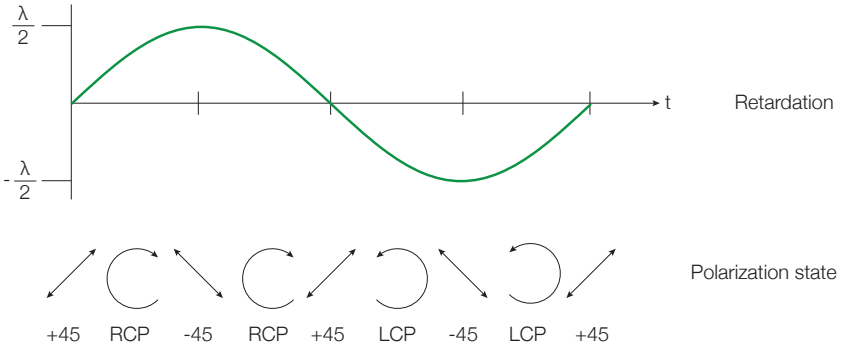

Figure 2.2.: A photoelastic modulator acting on a 45° LP incoming light beam. One period depicted above takes around 20μs. The retardation amplitude is set to $\lambda/2$.

ers and a lock-in amplifier, the PEM causes characteristic changes depending on polarization ellipticity and rotation that can be picked up with a detector. The mathematical description will be given in the next section.
Because of its high modulation frequency, the PEM/lock-in combination is rather insensitive to noise and allows for very accurate measurements.

Calculation for Our Setup

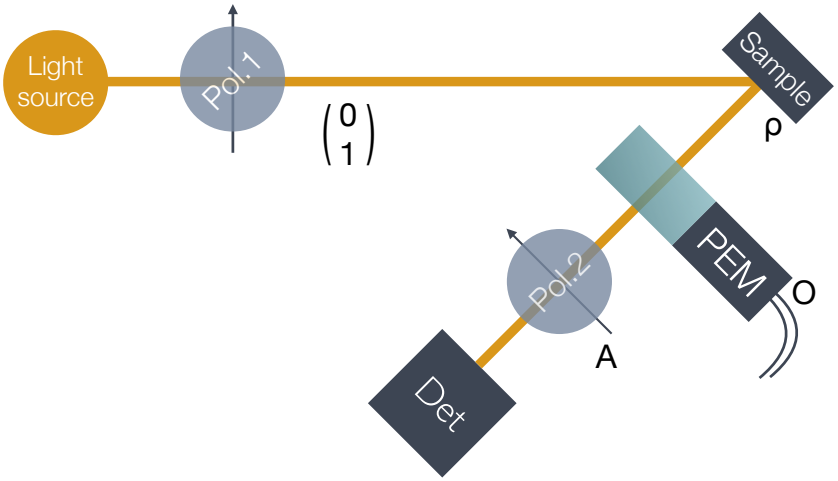

Figure 2.3.: Schematic of the polarizing elements in the setup. Monochromated light is polarized in the y-direction by polarizer 1, reflected by the sample, modulated by the PEM, passes polarizer 2 and is collected by the detector. The symbols of the Jones matrices are attached.

We can calculate the intensity measured at the end of the beam path by representing each optical element in figure 2.3 with its corresponding Jones matrix.
We start out with unpolarized monochromated light. The first polarizer is set to 90° with

respect to the x-axis and gives us light polarized in the y-direction, $\binom{0}{1}$, as a starting point. As introduced in section 1.2, the sample has different reflection coefficients for left and right circularly polarized light. In a circular basis, its Jones matrix is given by:

$$\rho_{\text{circ}} = \begin{pmatrix} \tilde{\rho}_+ & 0 \\ 0 & \tilde{\rho}_- \end{pmatrix}$$

Since we want to do the rest of the calculation in a Cartesian basis, we use the transformation matrices F and F^{-1} to switch representations:

$$\rho_{\text{Cartesian}} = F^{-1}\rho_{\text{circ}}F = \frac{1}{\sqrt{2}}\begin{pmatrix} 1 & 1 \\ -i & i \end{pmatrix} \cdot \rho_{\text{circ}} \cdot \frac{1}{\sqrt{2}}\begin{pmatrix} 1 & i \\ 1 & -i \end{pmatrix}$$

The PEM is a phase retarder as described in table A.1, with the addition that the amount of retardation is now a periodic function in time:

$$O = \begin{pmatrix} e^{i\frac{\delta}{2}} & 0 \\ 0 & e^{-i\frac{\delta}{2}} \end{pmatrix}, \qquad \delta(t) = \delta_0 \sin \omega t$$

The second polarizer (the analyzer) is set to an angle of 135° (or 45°). Other configurations are possible, but will yield a worse signal-to-noise ratio in most experiments[14]. Thus, our general expression is simplified:

$$A(135°) = \begin{pmatrix} \cos^2\frac{3\pi}{4} & \cos\frac{3\pi}{4}\sin\frac{3\pi}{4} \\ \sin\frac{3\pi}{4}\cos\frac{3\pi}{4} & \sin^2\frac{3\pi}{4} \end{pmatrix} = \begin{pmatrix} \frac{1}{2} & -\frac{1}{2} \\ -\frac{1}{2} & \frac{1}{2} \end{pmatrix}$$

Combining all the elements, the full Jones matrix representation of the beam path is:

$$\mathbf{E}_{\text{out}} = A \cdot O \cdot F^{-1} \cdot \rho_{\text{circ}} \cdot F \begin{pmatrix} 0 \\ 1 \end{pmatrix} \tag{2.1}$$

$$= \frac{1}{2} \cdot \begin{pmatrix} \frac{1}{2} & -\frac{1}{2} \\ -\frac{1}{2} & \frac{1}{2} \end{pmatrix} \begin{pmatrix} e^{i\frac{\delta}{2}} & 0 \\ 0 & e^{-i\frac{\delta}{2}} \end{pmatrix} \begin{pmatrix} 1 & 1 \\ -i & i \end{pmatrix} \begin{pmatrix} \tilde{\rho}_+ & 0 \\ 0 & \tilde{\rho}_- \end{pmatrix} \begin{pmatrix} 1 & i \\ 1 & -i \end{pmatrix} \begin{pmatrix} 0 \\ 1 \end{pmatrix} \tag{2.2}$$

$$= \frac{e^{-i\frac{\delta}{2}}}{4} \cdot \begin{pmatrix} ie^{i\delta}(\tilde{\rho}_+ - \tilde{\rho}_-) - (\tilde{\rho}_+ + \tilde{\rho}_-) \\ (\tilde{\rho}_+ + \tilde{\rho}_-) - ie^{i\delta}(\tilde{\rho}_+ - \tilde{\rho}_-) \end{pmatrix} \tag{2.3}$$

$$= \frac{e^{-i\frac{\delta}{2}}}{4} \cdot (ie^{i\delta}(\tilde{\rho}_+ - \tilde{\rho}_-) - (\tilde{\rho}_+ + \tilde{\rho}_-)) \cdot \begin{pmatrix} 1 \\ -1 \end{pmatrix} \tag{2.4}$$

The signal intensity arriving at the detector is the absolute squared of this value:

$$I_{\text{out}} = |\mathbf{E}_{\text{out}}|^2 \tag{2.5}$$

$$= \frac{1}{8} \cdot |ie^{i\delta}(\tilde{\rho}_+ - \tilde{\rho}_-) - (\tilde{\rho}_+ + \tilde{\rho}_-)|^2 \tag{2.6}$$

We note here that $\tilde{\rho}_+$ and $\tilde{\rho}_-$ are complex valued and of the form $\tilde{\rho}_\pm = r_\pm e^{i\theta_\pm}$. We also define $\Delta\theta = \frac{1}{2}(\theta_+ - \theta_-)$ After a lengthy calculation we receive:

$$I = \frac{1}{4}\left[r_+^2 + r_-^2 + (r_+^2 - r_-^2)\sin\delta + 2r_+r_-\cos\delta\sin\Delta\theta\right] \tag{2.7}$$

From equation 1.24 we take the relations $\theta_k = -\frac{1}{2}(\theta_+ - \theta_-) = -\frac{1}{2}\Delta\theta$ and $\epsilon_k = \frac{r_+ - r_-}{r_+ + r_-}$.
We estimate the difference in reflectivity to be small: $|r_+ - r_-| \ll r_+ + r_-$. This allows us to use the following approximations:

- $\frac{r_+^2 - r_-^2}{r_+^2 + r_-^2} \approx 2\frac{r_+ - r_-}{r_+ + r_-} = 2\epsilon_k$
- $\frac{r_+ r_-}{r_+^2 + r_-^2} \approx \frac{1}{2}$

Additionally, we use the shorthand $R = \frac{1}{2}(r_+^2 + r_-^2)$. This gives us the following simplified equation[1]:

$$I = \frac{1}{2}R\left[1 + 2\epsilon_k \sin\delta + \cos\delta\sin(-2\theta_k)\right] \tag{2.8}$$

Bessel Function Expansion

We are now able to write the signal as a function of the quantities we want to measure (θ_k and ϵ_k). However, until now they are superimposed. The strength of the polarization modulation technique lies in the fact that the two quantities can be extracted from the same signal simultaneously and with great sensitivity. We remember that the phase retardation δ is not a constant value but is periodically modulated by the PEM: $\delta(t) = \delta_0 \sin\omega t$. This allows a lock-in amplifier to separate the two.
Mathematically, we can show this by doing a Fourier decomposition on equation 2.8 that involves Bessel functions. We use the following identities (the proof can be found in the

[1] For an analyzer setting of 45° instead of 135°, the signs of the second and third term will be reversed.

appendix A.2):

$$\begin{aligned}\cos(\delta_0 \sin(\omega t)) &= J_0(\delta_0) + 2\sum_{n=1}^{\infty} J_{2n}(\delta_0)\cos(2n\omega t) \\ &= J_0(\delta_0) + 2J_2(\delta_0)\cos(2\omega t) + \mathcal{O}(J_4(\delta_0)), \qquad (2.9)\\ \sin(\delta_0 \sin(\omega t)) &= 2\sum_{n=0}^{\infty} J_{2n+1}(\delta_0)\sin((2n+1)\omega t) \\ &= 2J_1(\delta_0)\sin(\omega t) + \mathcal{O}(J_3(\delta_0)) \qquad (2.10)\end{aligned}$$

This allows us to expand the intensity in terms of frequency components, orders higher than

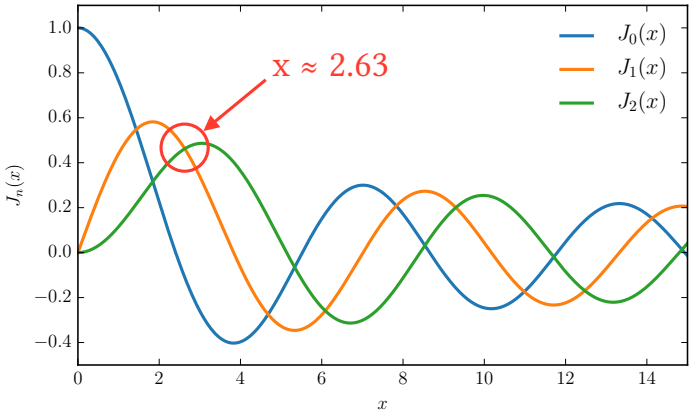

Figure 2.4.: Three Bessel functions of the first kind. The first intersection of J_1 and J_2 is circled, as we will use this value as a compromise for good signal-to-noise ratios in both ellipticity and rotation.

2ω are ignored. The component without temporally modulated intensity will be called $I(0)$.

$$I = I(0) + I(\omega) + I(2\omega) + \text{higher orders},$$

$$\begin{aligned}I(0) &= \tfrac{R}{2}(1 + 2J_0(\delta_0)\sin(-2\theta_k)), \qquad (2.11)\\ I(\omega) &= \tfrac{R}{2}(4J_1(\delta_0)\epsilon_k), \qquad (2.12)\\ I(2\omega) &= \tfrac{R}{2}(2J_2(\delta_0)\sin(-2\theta_k)) \qquad (2.13)\end{aligned}$$

The values of $I(\omega)$ and $I(2\omega)$ depend on the retardation amplitude δ_0. For values of 105.5° and 175° respectively, the Bessel functions of first and second order are at a local maximum, thus maximizing our measurable signals. To get strong signals for both, we pick a retardation amplitude of around 150.7° (2.63rad) which is at the first intersection of J_1 and J_2 (see figure

2.4).

Detectors and amplifiers may show different sensitivities to DC values and the modulated ω and 2ω signals which are in the kHz range. In the following, we will look at the actual measured signals (termed I_{DC}, I_f and I_{2f}) and introduce constants A and B to capture the dependence on the measurement apparatus. To extract the Kerr rotation and ellipticity, we will divide the PEM-modulated signals by the DC signal:

$$\frac{I_f}{I_{DC}} = A \cdot \frac{4J_1(\delta_0)\epsilon_k}{1 + 2J_0(\delta_0)\sin(-2\theta_k)} \approx 4AJ_1(\delta_0)\epsilon_k = \text{const.} \cdot \epsilon_k, \tag{2.14}$$

$$\frac{I_{2f}}{I_{DC}} = B \cdot \frac{2J_2(\delta_0)\sin(-2\theta_k)}{1 + 2J_0(\delta_0)\sin(-2\theta_k)} \approx -4BJ_2(\delta_0)\theta_k = \text{const.} \cdot \theta_k \tag{2.15}$$

We used the approximation $2J_0(\delta_0)\sin 2\theta_k \ll 1$ to get rid of the second term in equation 2.11 and the small angle approximation $\sin(-2\theta_k) \approx -2\theta_k$ to simplify equation 2.13. It should be noted that this holds well for typical small rotation angles below 1° we expect in e.g. Nickel but introduces a progressively larger error for bigger angles which should be kept in mind. Within this approximation, we now find a linear dependence between our Kerr angles and

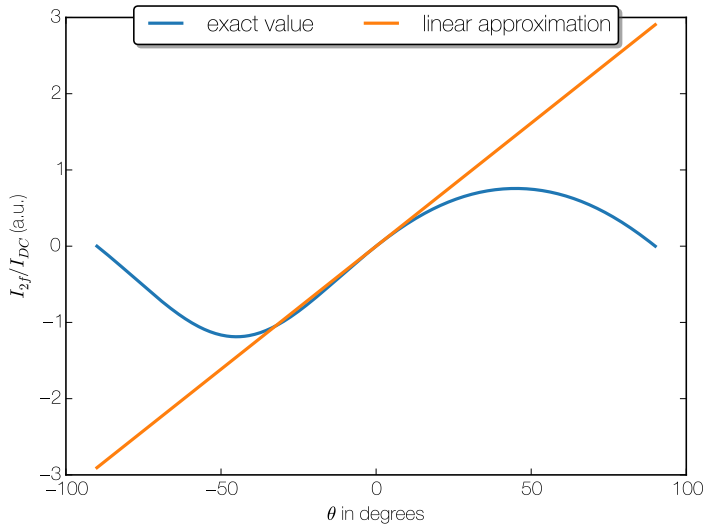

Figure 2.5.: Our linear approximation works only for small angles.

the fractions $\frac{I_f}{I_{DC}}$ and $\frac{I_{2f}}{I_{DC}}$. The constants that link these fractions to the actual values can be determined by calibration.

Calibration

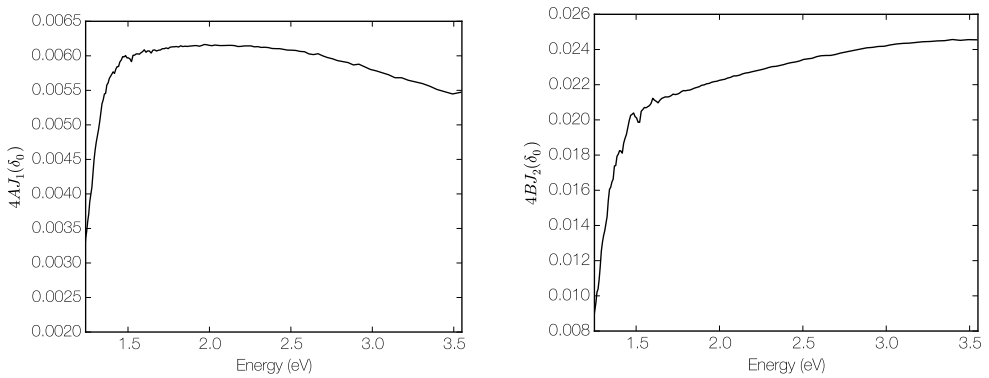

(a) Ellipticity calibration curve **(b)** Rotation calibration curve

Figure 2.6.: Example calibration curves. The spectra show how much the signal changes for a change of one degree.

Rotation

The calibration of the Kerr rotation is straightforward. The rotation of the first polarizer (see figure 2.3) creates a rotated linear polarization that influences the signal in the same way that a Kerr-active sample would. By turning this polarizer by a known and fixed amount ϕ_0, we can quantify the signal change that this rotation induces:

$$\left.\frac{I_{2f}}{I_{DC}}\right|_{\phi_0} = -4BJ_2(\delta_0)\phi_0 \tag{2.16}$$

By comparison with an angle $2\phi_0$ or the negative $-\phi_0$ we can determine the constant:

$$-4BJ_2(\delta_0) = \frac{\left.\frac{I_{2f}}{I_{DC}}\right|_{\phi_0} - \left.\frac{I_{2f}}{I_{DC}}\right|_{-\phi_0}}{2\phi_0} \tag{2.17}$$

Note that the detector may not have a constant response over the whole wavelength range to be measured. This makes $B = B(\lambda)$ a quantity that depends also on the wavelength of the light (see figure 2.6b).

Ellipticity

Calibration of the ellipticity is simple in theory: A quarter-wave plate (see table A.1) is placed in the beam path between the PEM and the second polarizer. It causes an additional phase retardation of $\frac{\pi}{2}$, thus modifying equation 2.8: By replacing δ with $\delta + \frac{\pi}{2}$, we receive $\cos\delta$ for $\sin(\delta + \frac{\pi}{2})$ and -$\sin\delta$ for $\cos(\delta + \frac{\pi}{2})$:

$$I = \frac{R}{2}\left[1 + 2\epsilon_k \cos\delta - \sin\delta \sin(-2\theta_k)\right] \tag{2.18}$$

Carrying out the same expansions and approximations as before will now yield:

$$4AJ_1(\delta_0) = \frac{\left.\frac{I_f}{I_{DC}}\right|_{\phi_0} - \left.\frac{I_f}{I_{DC}}\right|_{-\phi_0}}{2\phi_0} \tag{2.19}$$

In practice, this calibration is more difficult. Again, $A = A(\lambda)$ depends on the wavelength of the light, but standard quarter-wave plates are usually only specified for single wavelengths or for small spectral ranges. A Berek compensator can be used over a large wavelength range, but has to be adjusted by hand for each particular wavelength, which for our broad spectral range is tedious.

A solution to this particular problem is provided by a Fresnel rhomb (figure 2.7), which is achromatic over a large spectral range. Its major downside is that the beam exits the rhomb slightly below and/or to the side of its original position. This means that a realignment of the setup is necessary which should be avoided in measurement situations.

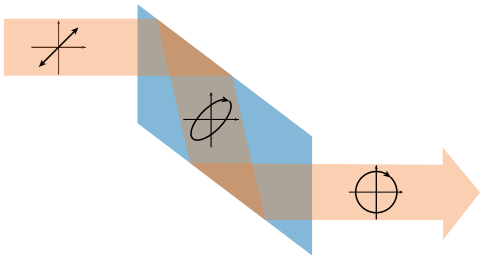

Figure 2.7.: For an incoming beam with 45° linear polarization, a Fresnel rhomb successively introduces a $\frac{\pi}{2}$ phase shift with two internal reflections. Unfortunately, the outgoing beam lies in a different plane.

3. Overview on Cu_2OSeO_3

3.1. Structure

Cu_2OSeO_3 is a magneto-electric[15] compound that hosts a skyrmion phase[16]. It shares the chiral and cubic B20 crystal structure with other discovered skyrmion compounds like MnSi and FeGe, but in contrast to these is an insulator. The different magnetic phases and the presence of a skyrmion lattice in this compound have been studied by means of small-angle neutron scattering[4]. This yields a rich phase diagram with the skyrmion phase located in a small pocket around 60K (see figure 3.1a). The crystal structure of Cu_2OSeO_3 is depicted in

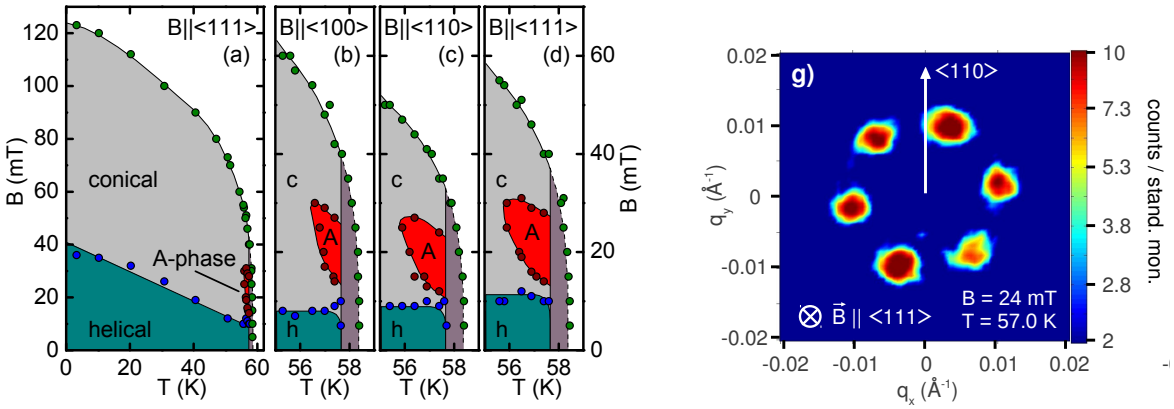

(a) Magnetic phase diagram for Cu_2OSeO_3. Below T_c, helical, conical, skyrmion and ferrimagnetic ordering is found depending on the external applied field.

(b) SANS image of the six-fold symmetry encountered in the skyrmion lattice phase, the magnetic field is aligned parallel to the neutron beam.

Figure 3.1.: Magnetic phases and a scan obtained with small-angle neutron scattering experiments performed on Cu_2OSeO_3 by Adams et al. [4]

figure 3.2a. There are two different kinds of copper sites in the unit cell, marked green and blue depending on the configuration of their oxygen ligands. The number of oxygen ions around the copper sites is the same in both cases, forming either a distorted square pyramid or a distorted trigonal bipyramid. This leads to different surroundings and a different crystal field splitting for the copper ions[15].

The copper ions are mainly responsible for the magnetic properties of Cu_2OSeO_3. Neglecting

the other constituents, there are four copper tetrahedra in the unit cell, see figure 3.2b. DFT calculations show that the interactions within these tetrahedra are strong and that neighboring tetrahedra are comparatively weakly coupled. This has led to a multi-scale approach to explain magnetic properties[17]: The tetrahedra are in a robust (excitation gap of ~275K) 3-up-1-down ground state and have an effective total spin of 1 (see figure 3.2b). The point is made that these rigid spin-1 clusters can be considered the building blocks of the magnetic structure and that the individual spins themselves are not of great importance at lower temperatures.

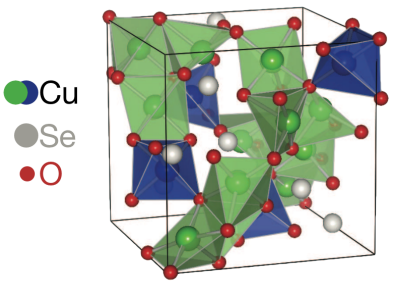

(a) Unit cell of Cu_2OSeO_3, adapted from [16].

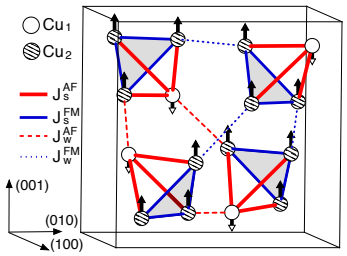

(b) Simplified picture of the Cu_2OSeO_3 unit cell. The relevant copper sites form tetrahedra. Figure from [18]

Figure 3.2.: Crystal structure of Cu_2OSeO_3

3.2. Magnetism in Cu_2OSeO_3

The interesting magnetic structures in Cu_2OSeO_3 and other B20 compounds are caused by the combination of different effects with different energy scales. Ferromagnetic coupling of spins (or, in this particular case, clusters) is the strongest ordering mechanism: It can be described by a Heisenberg Hamiltonian of the form:

$$H_{\mathrm{H}} = -\frac{1}{2}\sum_{\substack{i,j \\ i\neq j}} J_{ij}\mathbf{s}_i \cdot \mathbf{s}_j \tag{3.1}$$

For positive J_{ij} the system will prefer a parallel alignment of spins.
The crystal structure of Cu_2OSeO_3 belongs to the low-symmetry cubic $P2_13$ space group[19]. It contains a threefold rotation around $\langle 111 \rangle$ and a screw axis along $\langle 100 \rangle$, but lacks many common cubic symmetry operations. Most notably absent is inversion symmetry. This causes the crystal to be inherently chiral and is a condition for the occurrence of the Dzyaloshinskii-

Moriya (DM) interaction. Its basic Hamiltonian has the form:

$$H_{\mathrm{DM}} = -\frac{1}{2} \sum_{\substack{i,j \\ i \neq j}} \mathbf{D}_{ij} \cdot (\mathbf{s}_i \times \mathbf{s}_j) \tag{3.2}$$

Dzyaloshinskii predicted[20] in 1958 that in low-symmetry systems an antisymmetric exchange interaction of the form 3.2 can exist. Moriya worked out the microscopic theory two years later and found spin-orbit coupling to be a possible mechanism. In the simplest

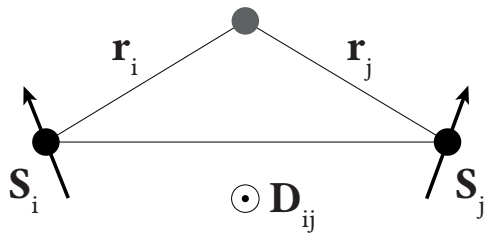

Figure 3.3.: Sketch of a DM geometry with one ligand.

case, the DM exchange interaction between two ions is mediated by a single third ligand (figure 3.3). The orientation of $\mathbf{D}_{ij}$ is perpendicular to the triangle spanned by the three ions: $\mathbf{D}_{ij} \propto \mathbf{r}_i \times \mathbf{r}_j$. If they are perfectly aligned, the cross product, and with it the DM interaction, is zero. The magnitude of the DM vector depends on the strength of the spin-orbit coupling in the material and is in general considerably smaller than J_{ij}.
The combination of Heisenberg and DM exchange interaction leads to the formation of twisted magnetic structures with a long period compared to the unit cell: The Heisenberg term wants to align the spins uniformly, the DM energy is minimized for $S_i \perp S_j$. The period of the magnetic helices is thus determined by the ratio $\frac{D}{J}$. [21]

Helical Phase, Conical Phase, Skyrmions

In zero or small applied magnetic field $B < B_{\mathrm{c1}}$ and below the critical temperature of around ~60K, Cu_2OSeO_3 is in a helically ordered magnetic state. Spins twist around a vector $\mathbf{q}$ as shown in figure 3.4a. The modulation period of the helices is 616 ± 45 Å, considerably larger than the unit cell. In contrast to MnSi, where the helical modulation is along ⟨111⟩, the helices are observed in the ⟨100⟩ directions at zero field[4]. Multiple domains of ⟨100⟩ helices with different directions coexist in this phase.
For slightly stronger fields $B_{\mathrm{c1}} < B < B_{\mathrm{c2}}$, the multi-domain structure aligns to the magnetic

field; the helices are now modulated along **B**. Additionally, the spins are no longer perpendicular to their common **q**-vector and start to align with the magnetic field. This results in a nonzero net magnetization along **B** (see figure 3.4b). The angle of the cone decreases with increasing magnetic field until a ferrimagnetically ordered state is reached at B_{c2}. For a small

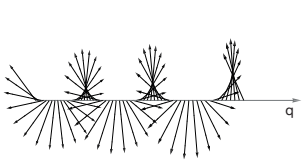

(a) Helical phase: The spins are perpendicular to the propagation vector **q** and twist around it.

(b) Conical phase: The spins are no longer perpendicular to the propagation vector but are slightly tilted towards **B**.

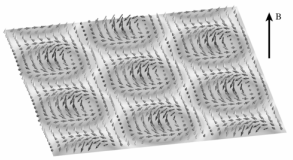

(c) Skyrmion phase: Ground state for a particular field and temperature region. Image from [22].

Figure 3.4.: Magnetic phases found in Cu_2OSeO_3

region of applied field and temperature around 30mT and 60K (see figure 3.1a), the skyrmion phase is the ground state of the system. These magnetic "knots" have gained considerable scientific attention, as they possess unique topological properties and are promising candidates for novel magnetic storage devices.

4. Measurements

4.1. Characterization of the Setup

Spectral Range and Wavelength Resolution

The light source used in the setup is a xenon arc lamp. The lamp glass is designed to cut off wavelengths below 300nm to reduce the amount of ozone produced in a lab setting. The detector specifications allow for a measurable range of around 350 to 1000nm. To remove higher-order reflections from the monochromated light, several long-pass color filters can be used. Lamp spectra taken with different filters in place can be found in figure 4.1. Automatic filter switching has been built into the measurement programs.

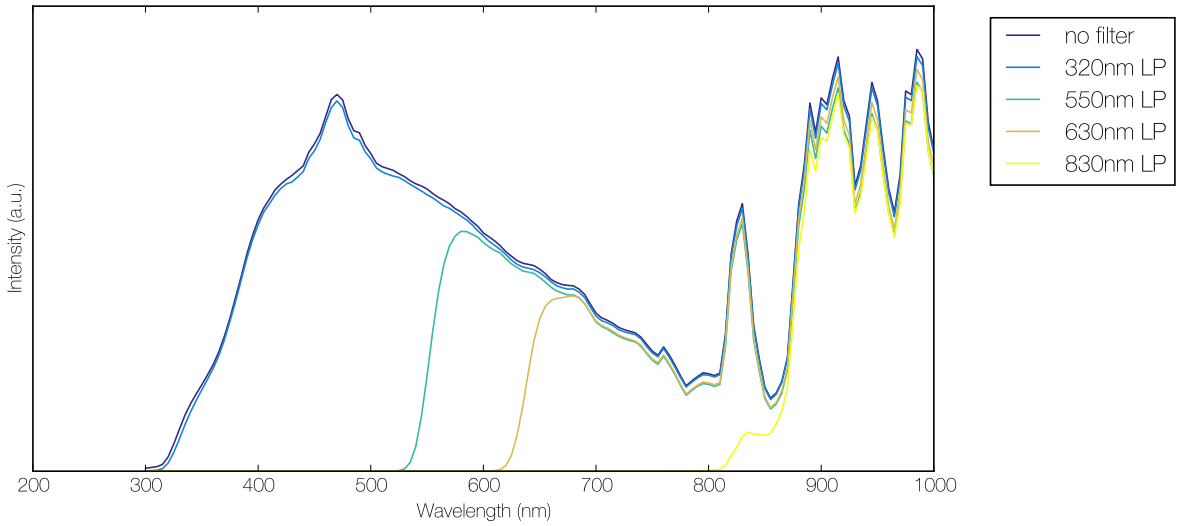

Figure 4.1.: Spectra as emitted by the Xe lamp and measured by the Thorlabs PDA100A photodetector. The available long-pass color filters are listed. Wavelength step size: 5nm.

With the two slits of the monochromator, one can change the linewidth of the monochromated light. Narrower slits lead to a smaller FWHM. An exemplary measurement has been done at a wavelength of 548nm: As can be seen in figure 4.2, there is a trade-off between light intensity and linewidth. The achievable range of FWHM at 548nm lies between ~20nm (for a slit width of 2mm) and ~3nm (for a slit width of 0.25mm). This limits our achievable wavelength resolution and should be changed in unison with the step size in the measurement

software for best results.

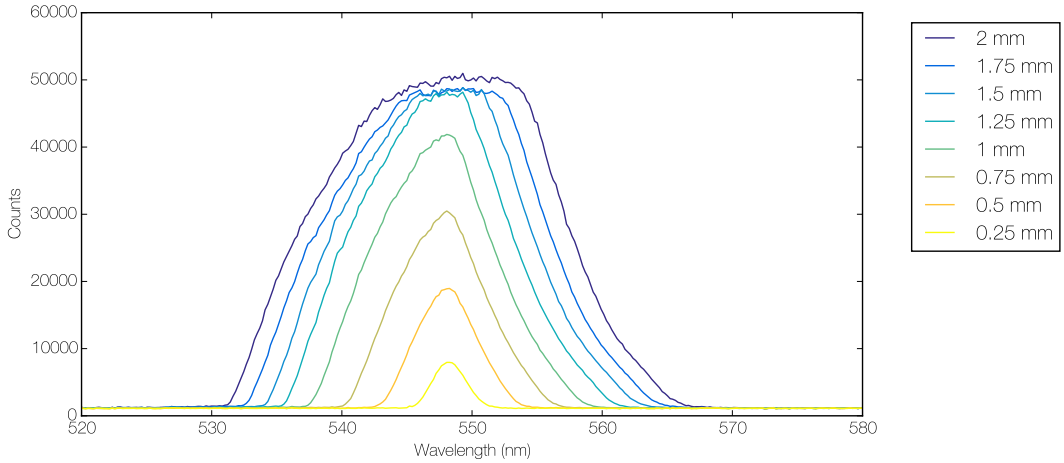

Figure 4.2.: Dependence of the linewidth of the monochromated light on the slit width; measured with an rgb lasersystems Qmini spectrometer.

Noise and resolution

The achievable resolution of our setup is limited by the the amount of noise in the measured quantities. In the Kerr geometry, the measured angles are usually small, so a good resolution is needed. To test the noise floor of the setup, we set the first polarizer to a particular rotation value and record the rotation signal in time, as reflected from a representative sample. Ideally, the fluctuations in the measured value should be as small as possible. The standard deviations σ_θ of the measured values were taken. Some exemplary values can be found in the table below. The settings of the entrance an exit slits give us an FWHM of around 15nm for the wavelength.

Wavelength (nm)	400	540	800
Standard deviation σ_θ (deg)	$6.15 \cdot 10^{-3}$	$3.58 \cdot 10^{-3}$	$13.01 \cdot 10^{-3}$

These values will depend on different factors:

Reflectivity: The values above were measured on a Cu_2OSeO_3 sample that shows only $\approx 2\%$ reflected intensity in comparison to an aluminum mirror. For a more reflective surface, the signal-to-noise ratio will be substantially better.

Integration time: Prolonging the integration time set on the lock-in amplifiers will reduce the noise level, with the cost of a longer measurement.

Stability: Vibrations in both sample and optics can increase the noise level. For example: In the measurements above, the vacuum pump of the cryostat was still running. If maximum sensitivity is crucial, all pumps can be turned off.

Lamp intensity: The intensity output of our light source is strongly wavelength-dependent (see figure 4.1). This will worsen the noise level in some regions of low intensity.

Test Measurement on Nickel

To test the measurement setup, we measured the Kerr rotation of Nickel, which displays a comparatively small Kerr rotation, using a polished polycristalline Nickel plate of around 5mm×5mm size. The measurement procedure is as follows:

- The Nickel plate is brought into magnetic saturation in an applied field B parallel to the incoming light
- The monochromator and PEM traverse the wavelength range with a predefined step size; I_{DC}, I_f and I_{2f} are recorded for every step
- The measurement is repeated for an applied field of -B

The Kerr rotation of Nickel is relatively small. Additionally, the beam path contains potentially birefringent elements like lenses that may cause a slight change in the measured values. We use that fact that the Kerr effect changes sign when the magnetic field is flipped and use the measurements at +B and -B to isolate the antisymmetric component:

$$\left(\frac{I_{2f}}{I_{DC}}\right)_{\text{antisym.}} = \frac{1}{2}\left(\left.\frac{I_{2f}}{I_{DC}}\right|_{+B} - \left.\frac{I_{2f}}{I_{DC}}\right|_{-B}\right) \tag{4.1}$$

This calculation also eliminates potential small misalignments of the polarizers and gives us a proper value for zero rotation. After this, the calibration terms as defined in section 2.2 are applied to the measurement values.
This results in a Kerr rotation as depicted in figure 4.3. Compared to values obtained by Krinchik[23] and van Engen[24], our values seem to be in good agreement. Little deviations are expected, because Krinchik and van Engen did measurements on single crystals.

4.2. Sample Preparation

The Cu_2OSeO_3 samples used were grown in Groningen by Aisha Aqueel and have diameters between 1 and 3 millimeters. The sample orientation and single-crystallinity was determined

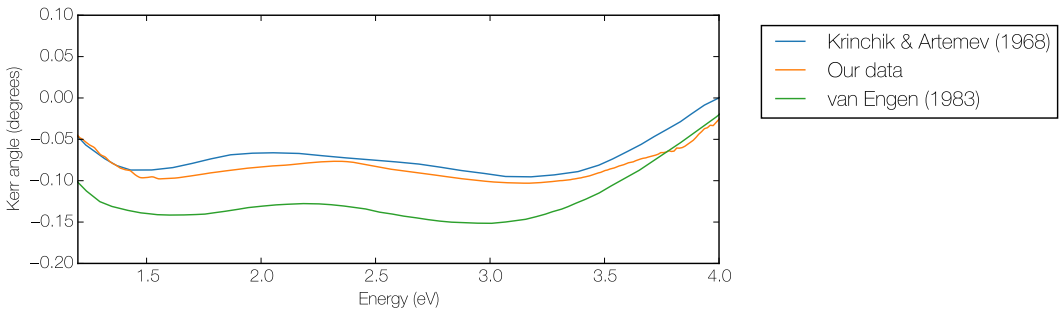

Figure 4.3.: Comparison of our test measurement on polycristalline Nickel and two measurements from literature (performed on single crystals). Our data has been smoothed with a Savitzky-Golay kernel with a window size of 20 data points.

in the institute's Laue machine. With the help of the CLIP software by O. Schumann[25], the scanned Laue patterns can be fitted if the space group and lattice parameters of the material are known (see figure 4.4a). For now, our setup only supports the polar configuration

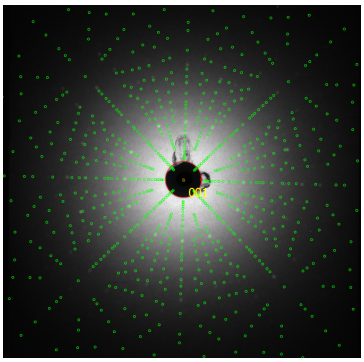

(a) Laue image created in the orientation process.

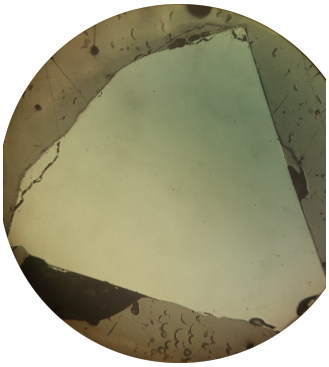

(b) [111] surface of sample 2 after lapping and polishing.

Figure 4.4.: Sample preparation: Laue image and close-up of the surface taken under a microscope.

(compare to figure 1.1), this means that we have to pick a crystal direction to which both the applied magnetic field and the incoming light beam are parallel. The [111] direction was chosen for two reasons: The skyrmion phase pocket seems to have the largest spread in this magnetization direction (see figure 3.1a). Because it is fairly small in both temperature and applied magnetic field, we wanted to maximize our chances of hitting it on purpose. Also, the magneto-electric effect induces an electric polarization $\mathbf{P} \parallel \mathbf{H}$ in this direction – for an applied field in the [100] direction no polarization appears. This may have interesting effects in the polarization behavior.

The samples were lapped and polished to achieve high reflectivity and little scattering (see

figure 4.4b). In the end, we had surface areas of around 1mm^2 for sample 1 and 3mm^2 for sample 2 to work with, which is big enough for our spectrometer spot size.
The samples were mounted on a copper plate next to a piece of aluminum mirror which functions as a reference material inside the cryostat.

	Sample 1	Sample 2
Orientation	[111]	[111]
Approximate diameter	1.5mm	3mm
Approximate thickness	0.4mm	1mm

4.3. Kerr Measurements

We began with measurements on sample 1. In the polarization rotation spectra at a temperature of 10K (see figure 4.5a), we find features around 1.55eV and 3.5eV that show a relatively big rotation but seem to be roughly proportional to the applied field, as is expected for the Kerr effect. However, we also find an exceptionally large rotation centered around 540nm/2.3eV that does not seem to behave linearly.
The smaller figures below show the dependence of the Kerr rotation on the applied field at two different energies. On the left, the B-dependence at 800nm seems to be roughly linear up to the saturation field. The two small bumps at ±40mT seem to correspond to the point B_{c1} in magnetization behavior where the different q-domains in the material become aligned and the sample enters the conical phase. The sudden change around ±170mT corresponds to the field B_{c2} where the spins in the material become ferrimagnetically aligned and a saturation is reached.
The lineshape[1] in figure 4.5c is very puzzling. It shares the ferrimagnetic saturation point with the 800nm measurement, but has two sinusoidal oscillation periods with a very large amplitude in between. It turns out that this is a combination of two effects – an explanation will be given in section 4.4.
In a temperature-dependent measurement (figure 4.6), we find that the features lose in intensity when going to the critical temperature and beyond. We estimate T_c to be around 56K for our sample[2]. The amplitude of the oscillations at 540nm decreases slightly with temperature, the period length seems to stay approximately constant. The ferrimagnetic saturation field

[1] In contrast to the spectrum above, this measurement starts at $\theta_k = 0$ for $B = 0$. This was a deliberate choice, as for this magnitude of polarization rotation, the small angle approximation we used in section 2.2 starts to become problematic. We thus wanted to spread the rotation above and below zero as equal as possible.
[2] This can be seen very nicely in the magnetic phase diagrams in the later section 4.5.

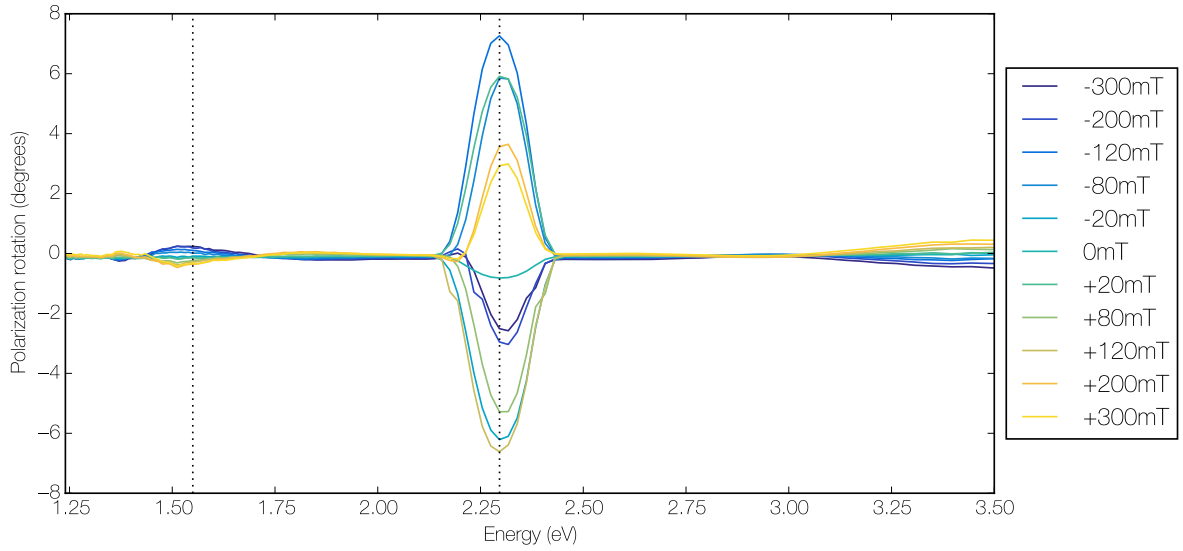

(a) Kerr rotation spectra at 10K for different magnetic field strengths. Detailed behavior at the dotted lines is shown in figures **(b)** and **(c)**.

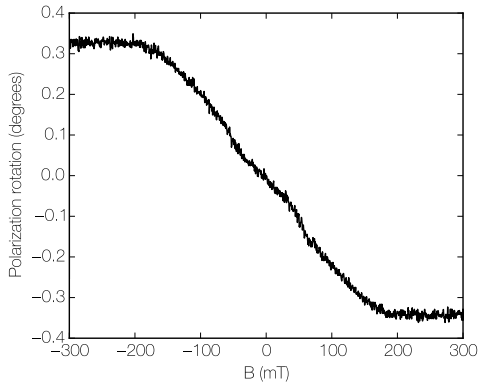

(b) The behavior at 1.55eV/800nm

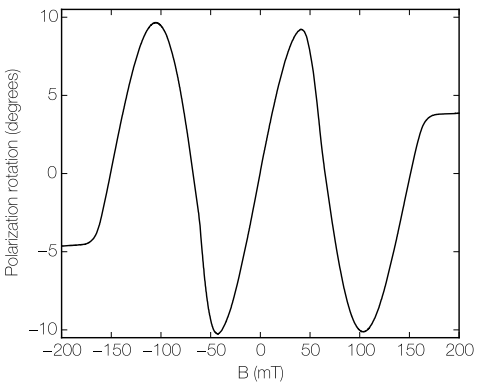

(c) The behavior at 2.3eV/540nm

Figure 4.5.: Kerr rotation spectra and magnetic field sweeps at 10K

B_{c2} decreases with temperature, which leads to the lineshape slowly being "eaten up" from the sides.

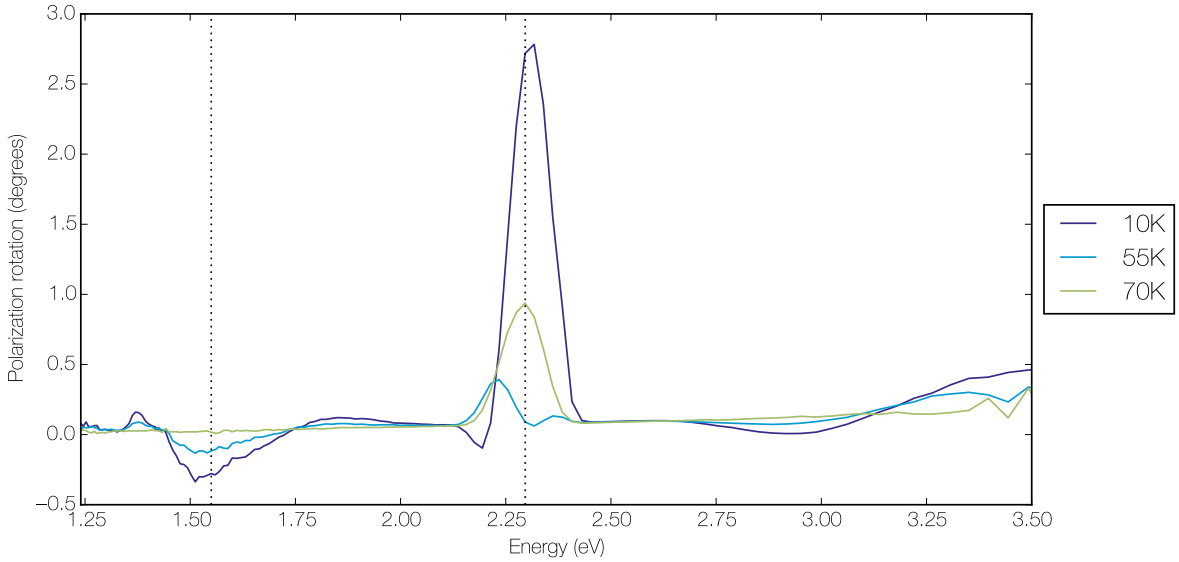

(a) Temperature dependence of the Kerr rotation spectra for B=300mT

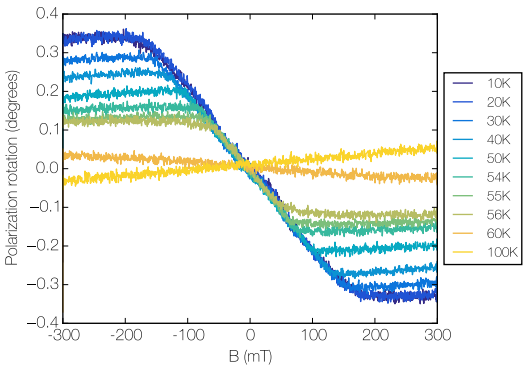

(b) The behavior at 1.55eV/800nm for different temperatures.

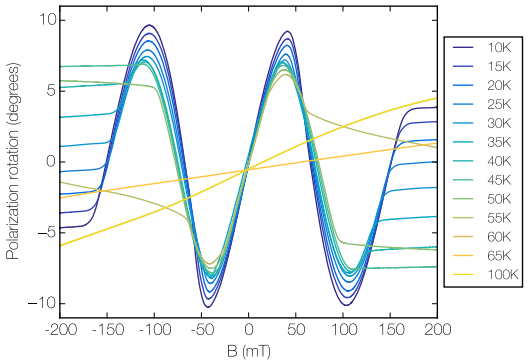

(c) The behavior at 2.3eV/540nm for different temperatures.

Figure 4.6.: Kerr rotation spectra and magnetic field sweeps for different temperatures.

Transmission

The needed clue to explain the strange lineshape around 540nm came with the measurement of the thicker second sample. There, the large irregular peak seems to be missing. A closer investigation reveals that the peak is not completely gone but just much weaker in amplitude. Also, now there are more oscillations in the region between $-B_{c2}$ and B_{c2} (see figure 4.8a). An explanation is that the light can transmit through the sample at this particular wavelength and is Faraday-rotated. This had previously not been taken into account, because the crystal seemed fully opaque at room temperature. As measurement 4.7a shows, there is indeed a narrow transmission window progressively opening for lower temperatures.
The progression of the absorption coefficient α from $\frac{I_{\text{transm.}}}{I_0 - I_{\text{refl.}}} = e^{-\alpha \cdot l}$ at a wavelength of 540nm is given in figure 4.7b. This should be considered an estimate: The exact measurement of the sample thickness was not possible during the end phase of this thesis and is assumed to be 1mm±20%. The reflectance is set to 2% based on some earlier comparisons with an aluminum mirror, but will of course depend on the surface quality.

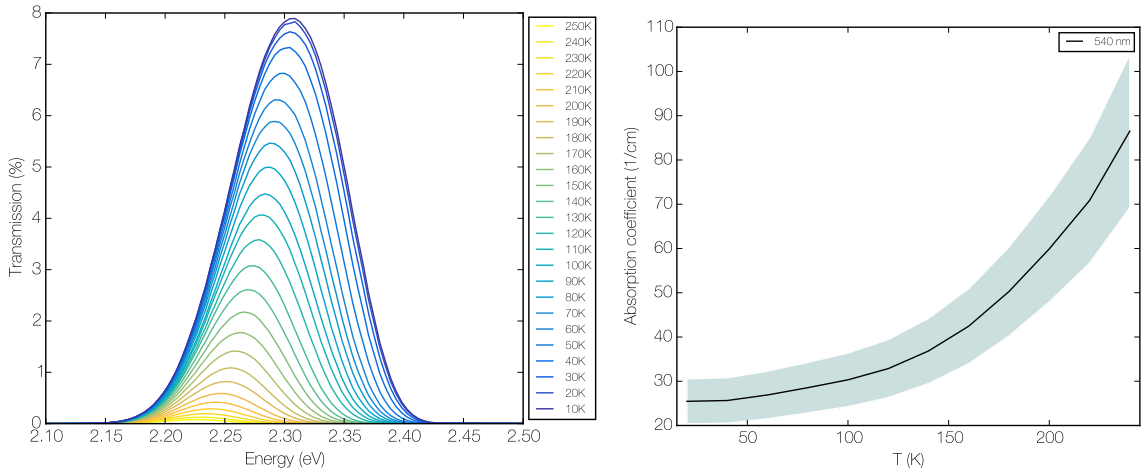

(a) For lower temperatures, a narrow transmission window opens. Measured on sample 2.

(b) Estimation of the absorption coefficient for 540nm light. An error of 20% is given for the sample thickness.

Figure 4.7.: Transmission properties for different temperatures.

To find out more about the optical properties of Cu_2OSeO_3, a preliminary ellipsometry measurement was carried out by I. Vergara and can be found in the appendix A.3. Unfortunately, no low temperature ellipsometry data was available during the writing of this thesis. This also prohibits us from calculating the full dielectric tensor.

4.4. Modelling the Results

Inspired by the transmission measurement and the Kerr data of sample 2, one can find a phenomenological model for the rotation curves of section 4.3. Because the material becomes

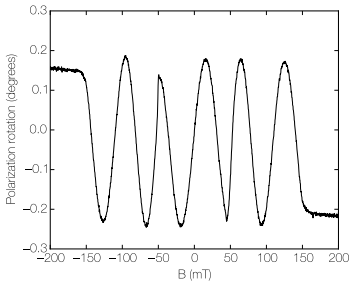

(a) For a different, thicker sample the field sweep around 540nm revealed more oscillations. This was a clue that transmission and Faraday rotation are happening.

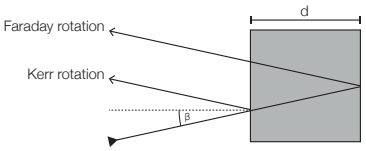

(b) The outgoing beam consists of a reflected, Kerr rotated part and a partially transmitted and back-reflected part that experiences Faraday rotation.

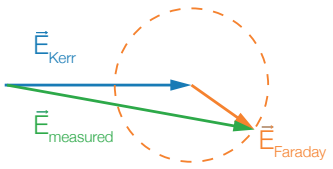

(c) The field vectors of reflected and partly transmitted light add up to the measured end result.

Figure 4.8.: An explanation for the nonlinear curves of section 4.3

transparent at around 2.3eV for lower temperatures, part of the incoming light can now traverse the material and gets reflected from the backside of the crystal (see figure 4.8b). While the part of the ray that is reflected on the front experiences a normal (presumably small) Kerr rotation, the part reflected from the back experiences a Faraday rotation over a length of $2d/\cos\beta$, where d is the thickness of the crystal and β is the angle of the incident light relative to the surface normal. The Faraday rotation is field-dependent and can be described via the linear relation

$$\begin{aligned}\theta_f &= M(H) \cdot V \cdot l \\ &= M(H) \cdot V \cdot \frac{2d}{\cos\beta}\end{aligned} \tag{4.2}$$

Here, V is the Verdet constant with units $[\frac{\text{rad}}{T \cdot m}]$, describing the amount of polarization rotation per length per field. As further measurements will show, the Verdet constant is extraordinarily large in Cu_2OSeO_3. Viewed from the point of the detector, we see a combination of two electric field vectors: The Kerr-rotated, front-reflected one that shows only a minimal field dependence and the Faraday-rotated, back-reflected one that strongly rotates depending on the applied field. The measurement apparatus picks up the sum of the two and this leads to

the periodic B-dependence we see in the magnetic field sweeps (see figure 4.8c). Note that this also explains the different result for the thicker sample: Here, the path through the crystal is longer, thus the Faraday rotation is stronger but the back-reflected intensity is weaker. Thus we see more oscillations and an overall weaker oscillation amplitude.
In summary, we assume the following for our model:

1. We impinge on the sample with fully s-polarized light.
2. For the sake of simplicity we consider only one back-reflection.
3. Absorption in the material follows a Lambert-Beer law: $I \sim e^{-\alpha \cdot l}$
4. Both Kerr and Faraday effects are linear in magnetization: $\theta_f = \frac{2M(H)Vd}{\cos\beta}$, $\theta_k = C_k M(H)$

One can choose either a complex number or a vector representation for the description of the model. The former one is shorter to write out but here we chose the latter, as it is more consistent with the Jones calculus used in the rest of the thesis.
For the Kerr-rotated part, the relationship is:

$$\mathbf{E}_k = r \cdot R[\theta_k(M(H))] \cdot \begin{pmatrix} 0 \\ 1 \end{pmatrix} \tag{4.3}$$

Here, R is a rotation matrix and r is the reflection coefficient[3]. For the Faraday-rotated part, we get:

$$\mathbf{E}_f = r(1-r)^2 \cdot e^{-\frac{\alpha \cdot 2d}{\cos\beta}} \cdot R[\theta_f(M(H))] \cdot \begin{pmatrix} 0 \\ 1 \end{pmatrix} \tag{4.4}$$

The measured Jones vector then is the sum of the two: $\mathbf{E}_{\text{tot}} = \mathbf{E}_k + \mathbf{E}_f$. To receive the change of the total polarization angle, we calculate the angle of the sum vector to the x-axis and subtract the 90 degrees we started out with:

$$\Delta\theta = \sphericalangle(\mathbf{E}_{\text{tot}}, \hat{\mathbf{x}}) - \frac{\pi}{2} = \arccos\left(\frac{\mathbf{E}_{\text{tot}} \cdot \hat{\mathbf{x}}}{|\mathbf{E}_{\text{tot}}|}\right) - \frac{\pi}{2} \tag{4.5}$$

The magnetization $M(H)$ of the sample rises approximately linearly up to the ferrimagnetic saturation point, from where on it stays almost constant. As a starting point, this could be

[3] If we want to be precise, we have to distinguish between s- and p-reflectivity, especially for the back-reflected light from inside the sample. For the sake of this model, this is close enough.

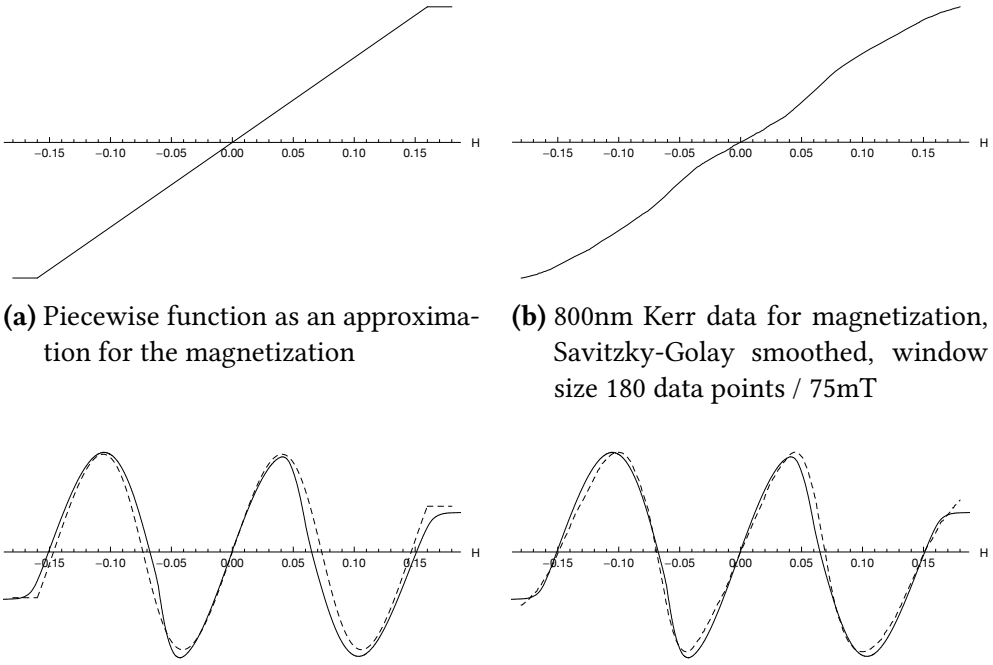

(a) Piecewise function as an approximation for the magnetization

(b) 800nm Kerr data for magnetization, Savitzky-Golay smoothed, window size 180 data points / 75mT

(c) Model resulting from the piecewise function above

(d) Model resulting from the 800nm data

Figure 4.9.: Using the model described in section 4.4 (dotted lines) we try to replicate the lineshape of the 540nm data.

approximated with a piecewise function (see also figure 4.9a):

$$M(H) = \begin{cases} -\tilde{C} \cdot H_{\text{sat}}, & H < -H_{\text{sat}} \\ \tilde{C} \cdot H, & -H_{\text{sat}} < H < H_{\text{sat}} \\ \tilde{C} \cdot H_{\text{sat}}, & H > H_{\text{sat}} \end{cases} \tag{4.6}$$

This, in combination with the model above, yields a fairly accurate representation of the lineshape (figure 4.9c). If we assume that the amount of Kerr rotation around 1.5eV/800nm is proportional to the actual magnetization of the sample, we can try to improve our fitting with this information. Using the data in figure 4.9b as the magnetization lineshape, we receive the fit of figure 4.9d. In conclusion, we feel confident that transmission and back-reflection is indeed what is causing the peculiar lineshape measured around 540nm.

4.5. Magnetic Phase Diagram

Although the polarization rotation data we collected around 540nm is a combination of two effects, we can still extract useful information from it. Similar to the work of T. Adams et al.[4] who found a skyrmion kink (see figure 1.3) in the derivatives of their SQUID magnetization data, we do the same in our Kerr/Faraday curves. For this, we take the first and second derivatives[4] of the polarization rotation at 540nm for all the measured temperatures. An example is given in figure 4.10: The derivative of the rotation at 54.7K shows features around ±25mT that are not present in the 51K data (marked with a dotted red line).
If we plot this region of interest for the temperature range of 54K to 56K, we see a feature fading in at around 30mT/54K and fading out again at 10mT/56K (figure 4.11). Subtle changes are also observed around 35mT. This corresponds to the boundaries of the skyrmion region as seen by Adams et al.

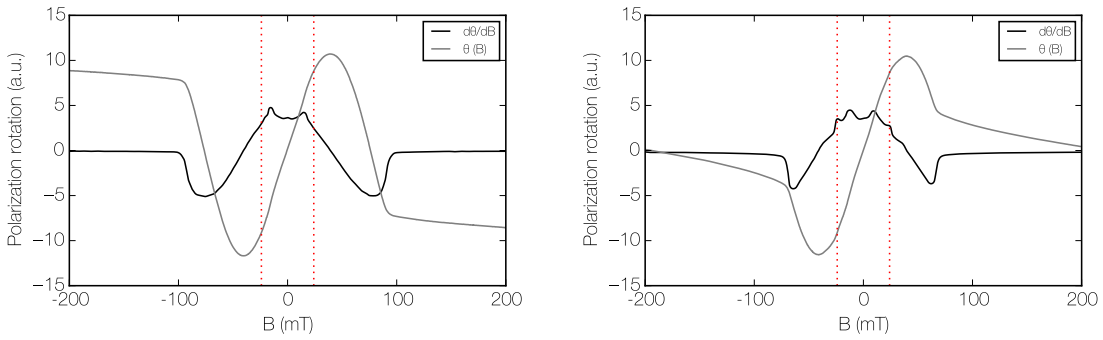

(a) 51K **(b)** 54.7K

Figure 4.10.: Example derivatives of the rotation data at 540nm. A difference in the derivative around a field of 30mT is observed.

To put the measurements in perspective, an efficient way of displaying this data is a 2D plot in which each column corresponds to a temperature, the y-axis is the applied magnetic field and the magnitude of the signal is given by the color. These color bar diagrams are given in figures 4.12 (a)-(e). This way, we receive a magnetic phase diagram: At points where the magnetization deviates from the continuous behavior because of a first/second order phase transition, there will be a corresponding deviation in the polarization rotation. This is made visible by taking the derivatives.
The phase diagram corresponds well to figure 3.1a, slight differences in the critical fields may

[4]The derivatives were calculated with the TVDiff algorithm described in [26]. It allows taking the derivative of noisy data without previous smoothing.

be due to a different sample shape and consequently different demagnetization factor.

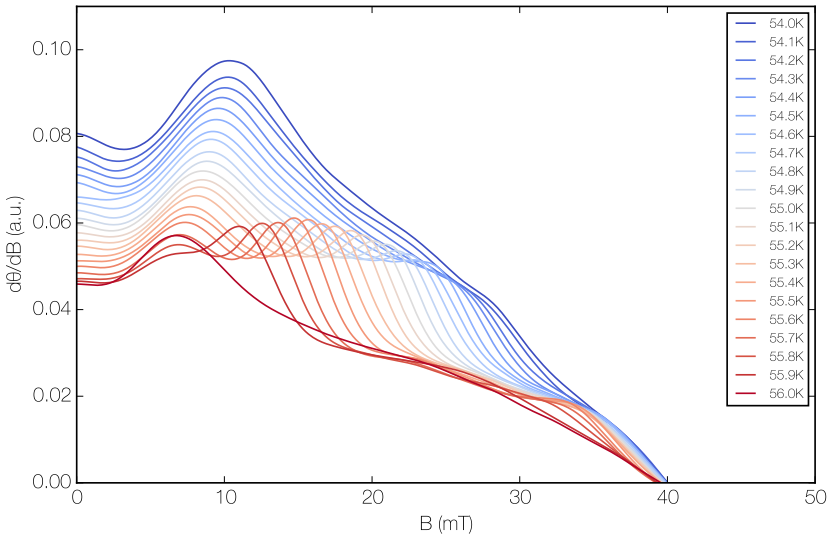

Figure 4.11.: A closer look at the first derivative of the rotation for small magnetic fields.

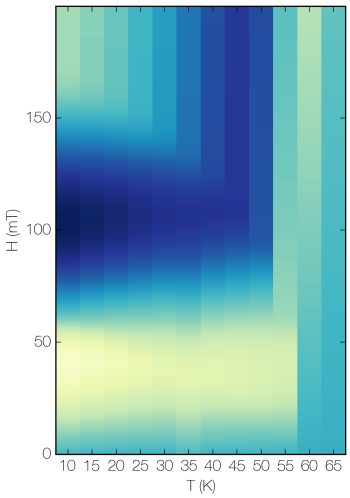

(a) The curves of figure 4.6c mapped qualitatively with colors. Each column corresponds to one measurement.

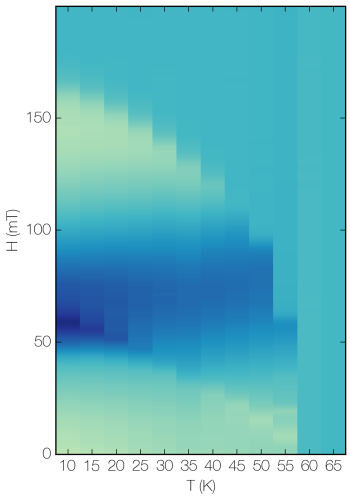

(b) First derivative of the data, a structure gets visible.

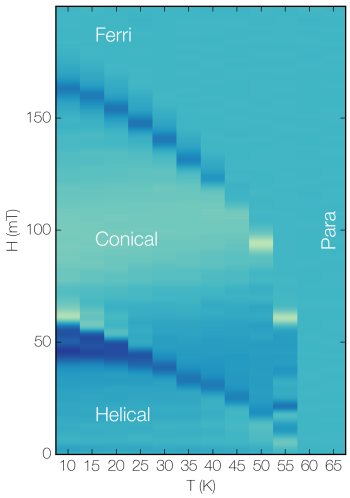

(c) Second derivative of the data, kinks in the original structure are now visible as peaks. This leads to a magnetic phase diagram.

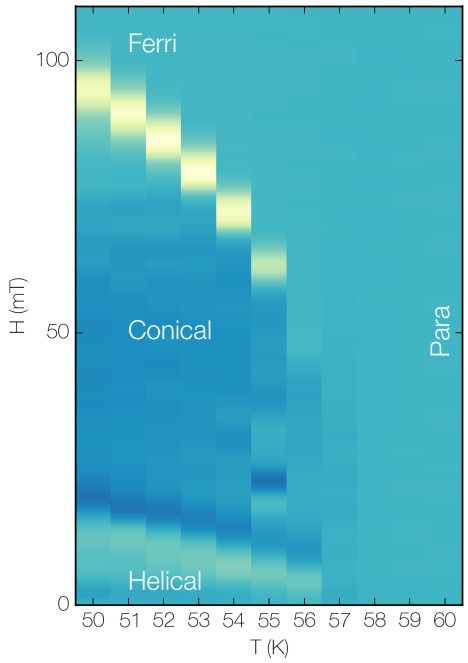

(d) Second derivative. Detailed view over a narrower temperature range. There seems to be an irregularity around 55K.

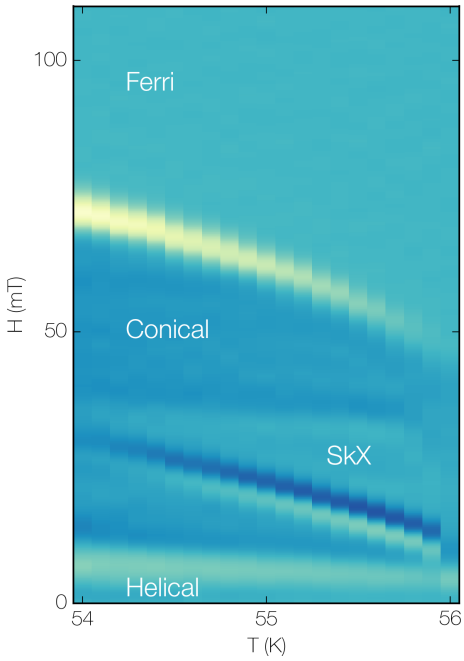

(e) Second derivative. Detailed view of the temperature region around 55K. The marked region corresponds to the skyrmion phase.

Figure 4.12.: The generation of a magnetic phase diagram from the polarization rotation data. The similarity to figure 3.1a is apparent. The scale is qualitative, light yellow corresponds to high values, dark blue to low ones.

Assignment of Transitions

Assigning internal optical transitions to the measured features is challenging because the internal electronic structure of the compound is not fully known. The selenium ions in the compound have filled d-orbitals, which leaves us with the copper and oxygen ions as possible participants for transitions. Figure 4.13 shows a sketch of the crystal field splitting on the two different copper sites. Due to the additional distortions[15] of the square pyramidal/trigonal bipyramidal oxygen ligand geometry, the d-levels will most likely be fully nondegenerate. The oxygen p-levels will certainly mix with the copper orbitals, but the exact hybridization mechanism and the resulting energy levels are not fully known.
Disregarding the energy levels, we can imagine three kinds of optically induced transitions in this system: An oxygen ligand electron jumping to a predominantly copper orbital is known as a charge transfer (CT) transition. In transition metal compounds these broad transition bands usually start in the blue/UV region of the spectrum. The features visible in the ellipsometry data (figure A.5) at 4/5.5eV and possibly also the one at the upper edge of the MOKE spectra (figures 4.5a and 4.6a) may mark the onset of the CT region.

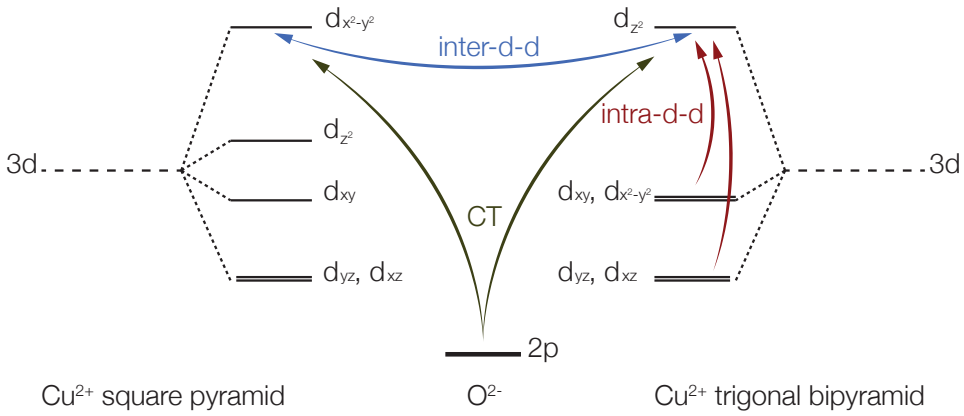

Figure 4.13.: Crystal field splittings of the two differently coordinated copper ions. Transitions from the oxygen p-levels are also possible.

The transfer of an electron between the two different copper sites is known as an inter-d-d transition. In DFT calculations[27], it is shown that the two different copper sites are antiferromagnetically coupled, thus no spin flip is needed to make the transition between the two highest orbitals.
Transitions between the split d-levels of one ion are usually forbidden due to symmetry. However, due to the crystal field distortions and the low-symmetry arrangement of the oxygen ligands, these intra-d-d transitions may become possible. The features in the lower part

of the measured spectra may correspond to either of these d-d transitions.
The transmission window around 2.3eV is likely the interval between two transitions. Here, the influence of the neighboring oscillators is high enough to induce a Faraday rotation, but the oscillator strength is sufficiently low to allow high transmission at this point. Improved DFT calculations and the consideration of the cluster model may help shine light on these processes.

4.6. Faraday Measurements

We continued with Faraday measurements on sample 2 which was previously polished from both sides to get optimum transmission. The Faraday rotation values measured around 540nm are indeed large, as we previously suspected in section 4.4. This is problematic, since we rely on the small angle approximation at a very early stage of our measurement setup (see section 2.2). However, there are three ways in which we can get information on the rotation behavior:

1. Beyond the range of a few degrees, the linear relation between the signal output and the actual rotation angle is no longer valid. However, we know that the ratio $\frac{I_{2f}}{I_{DC}}$ as output by the detector has a π-periodic angle dependence (see also figure 2.5). Because of this, we can estimate the angle between two maxima (or any two points with the same phase) to be around 180 degrees.

2. Additionally, we can measure the slope of the signal in a small angle region, for example in the interval [-5mT,5mT]. This will give us a value in terms of $\frac{\text{deg}}{\text{mT}}$ that we can use to extrapolate.

3. We can remove the PEM from the setup and just use two crossed polarizers. This will result in a $\sin^2$-like curve. With a fit function or by measuring the distance between two maxima one can read off which change in magnetic field causes a rotation of 180 degrees.

The following values should be considered estimates. For an exact determination, a thinner sample is needed to produce smaller rotations, which at the time of this thesis was not available.

Verdet Constant

For technical applications such as optical isolators (also known as optical diodes), it is beneficial to achieve large polarization rotations over a short distance. The phenomenological constant determining this rotatory "power" is the Verdet constant with units $[V] = \frac{\text{deg}}{\text{cm}\cdot\text{T}}$ or similar. In paramagnetic and diamagnetic materials with negligible magnetization, this constant is given in terms of the externally applied magnetic field. However, in ferro- and ferrimagnets, there is strong internal magnetization and the exact magnetization behavior is not always linear or even known. For these materials, it is common[28] to define a specific Verdet constant $\rho_\text{F} = \frac{\theta_F(M_s)}{l}$, which is the Faraday rotation at saturation magnetization M_s per length of the material traversed.

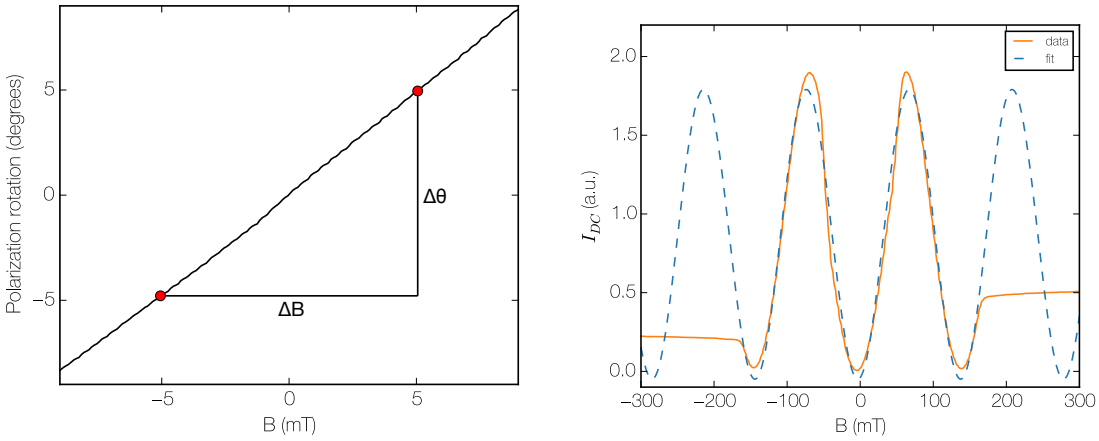

(a) Determination of the slope in a small field interval: $\frac{\Delta\theta}{\Delta B} = 0.964\frac{\text{deg}}{\text{mT}}$

(b) Signal measured with crossed polarizers (without PEM). A fit with the function $f(B) = y_0 + A\sin^2\frac{\pi}{\omega}(B - B_0)$ yields $\omega = 141$.

Figure 4.14.: Measurement of the Faraday effect at 10K and 540nm

We used methods 2 and 3 in figure 4.14. For this particular sample, method 2 yields a value of $\frac{\Delta\theta}{\Delta B} = 0.964\frac{\text{deg}}{\text{mT}}$, method 3 gives a slightly larger value of $1.277\frac{\text{deg}}{\text{mT}}$. This shows that the magnetization behavior is not linear, as expected. To estimate the effective Verdet constant at saturation magnetization, method 3 seems more appropriate, as it spans a larger field range in its calculation.

If we assume the sample to be 1mm thick and the saturation value to be at 165mT, we receive

a value of:

$$\rho_F(540\text{nm}, 10\text{K}) \approx 2100 \frac{\text{deg}}{\text{cm}} \tag{4.7}$$

For optical isolators, it is also desirable to have as little of the beam absorbed as possible. A figure of merit for these types of devices can thus be given by the ratio $\eta = \frac{\rho_F}{\alpha}$, where α is the absorption constant for the material at a particular wavelength. We can do a better estimation of the figure of merit than for the effective Verdet constant, because the sample thickness cancels out of the equation. Based on our measurements, it is given by:

$$\eta(540\text{nm}, 10\text{K}) = 2100 \frac{\text{deg}}{\text{cm}} / 25.4 \frac{\text{dB}}{\text{cm}} = 82.7 \frac{\text{deg}}{\text{dB}} \tag{4.8}$$

Commonly used materials in Faraday isolators are TGG (terbium gallium garnet, $Tb_3Ga_5O_{12}$) for the optical range and YIG (yttrium iron garnet, $Y_3Fe_5O_{12}$) for the near infrared. TGG is a paramagnet with a Verdet constant of -76.78 $\frac{\text{deg}}{\text{T·cm}}$ at a wavelength of 632nm at room temperature [29]. It is outclassed by two orders of magnitude at low fields by Cu_2OSeO_3, albeit at very different temperatures. In the near infrared, there are different doped YIG compounds that show an even higher effective Verdet constant. Some exemplary values can be found in table 4.15. The figure of merit values measured for Cu_2OSeO_3 rank above

Material	Wavelength λ (nm)	Specific rotation ρ_F (° cm^{-1})	Absorption coefficient α (dB cm^{-1})	Figure of merit ρ_F/α (° dB^{-1})
Fe[a]	546	3.5×10^5	3.3×10^6	0.11
Co	546	3.6×10^5	3.7×10^6	0.10
Ni	400	7.2×10^5	9.1×10^5	0.79
MnBi	632.8	5.3×10^5	3.3×10^6	0.16
YIG[b]	1064	280	65	4.3
	1150	250	54	4.6
	1200	240	50	4.8
	1310	224	35	6.4
	1550	216	23.8	9.1
YbBi : YIG[c]	1310	760	38	20
	1550	404	15.7	25.8
Bi : YIG[d]	1550	−1250	2.7	463
Ce : YIG[e]	1310	−2510	9.8	256
	1550	−1310	2.7	486

Figure 4.15.: A list of specific Verdet constants and figures of merit of several ferri-/ferromagnets. Table from [28]. All values are at room temperature.

undoped YIG compounds, although it has to be taken into account that the values in table 4.15 are given at room temperature. For higher temperatures, the absorption coefficient of Cu_2OSeO_3 rises, reducing its figure of merit considerably. Also, the large rotation ceases above T_C, which makes an application above 60K unrealistic at this point.

5. Conclusion and Outlook

During the course of this thesis, a polarization spectrometer was constructed and characterized. The setup gives good results that are in agreement with results from the literature. The measurements performed allowed us to gain an insight into the magnetic phases of Cu_2OSeO_3 in a purely optical way. Also, the goal of finding signatures of the skyrmion phase using polarization optics was reached. At low temperatures, Cu_2OSeO_3 was shown to have a fairly high Verdet constant and high transmission in an energy region around 2.3eV.
To move forward, it would be preferential to continue the measurements with thinner samples of different orientations. Then, high resolution Faraday measurements could be carried out with the PEM in place. With the help of low-temperature ellipsometry data, one could calculate the full dielectric tensor and learn more about the oscillators and transitions that lead to the optical phenomena we observe.
Although an application of the material in a Faraday rotator would certainly be possible because of its high rotatory power in the optical range, its low critical temperature of around 60K probably prevents Cu_2OSeO_3 from becoming a competitor to the wide-spread YIG and TGG systems. A change in the magnetic properties and the position of the transmission window might be achieved with doping. Also, the investigation of thin-film Cu_2OSeO_3 should be an interesting endeavor as well, especially since a MOKE measurement would be ideally suited for this type of sample.
A logical next step would be the realization of time-resolved MOKE or Faraday measurements: Characteristic magnons have been identified in Cu_2OSeO_3 in microwave studies[30], which should be visible as decay channels in a time-resolved measurement.
Apart from the multitude of different possibilities with Cu_2OSeO_3, the polarization spectrometer setup can also be used to study other materials with interesting magnetization behavior. A useful addition to the setup would be a more flexible magnet to measure other configurations such as transversal and longitudinal MOKE. Also, the use of a different detector would enable us to conduct measurements in the near-infrared spectral region.

A. Appendix

A.1. Parabolic Mirrors and Polarization Optics

Curved mirrors such as the off-axis parabolic mirror discussed here are ideal for many optical applications: Their focusing properties are based on the shape of the mirror surface, thus they do not suffer from chromatic aberrations like lenses, which have a wavelength-dependent focal length. An off-axis parabolic mirror is a cutout of a parabola that inherits

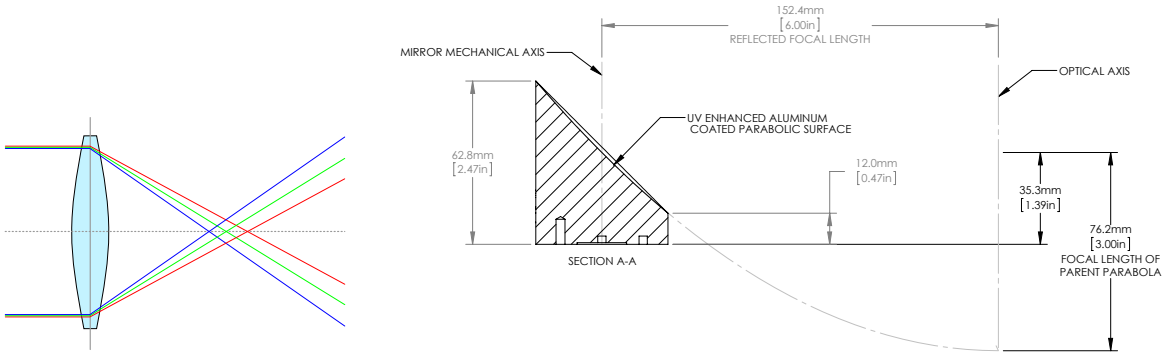

(a) Chromatic aberration of a convex focusing lens, image from [31].

(b) Geometry of an off-axis parabolic mirror, adapted from a Thorlabs data sheet[32].

Figure A.1.: Curved mirrors do not display chromatic aberrations.

its reflected focal length from the larger parent parabola (compare to figure A.1b). Collinear light coming from the positive z-direction is focused towards the optical axis of the parent parabola. When reflected from a smooth surface, the angle between the incoming beam and the surface normal is equal to the angle between the outgoing beam and the surface normal. Also, in- and outgoing beam lie in the same plane, the plane of incidence. In vector notation, this reads:

$$\mathbf{k}_{\text{out}}(\mathbf{k}_{\text{in}}, \hat{\mathbf{n}}) = \mathbf{k}_{\text{in}} - 2(\mathbf{k}_{\text{in}} \cdot \hat{\mathbf{n}}) \cdot \hat{\mathbf{n}} \tag{A.1}$$

Here, $\hat{\mathbf{n}} = \frac{\mathbf{n}}{|\mathbf{n}|}$ is the normalized surface normal and $\mathbf{k}_{\text{in/out}}$ are the in and outgoing propagation vectors of the light. With this, one can model the behavior of a parabola cutout[1] and can indeed find that collimated incoming rays are focused in a point **F** (figure A.2). We would

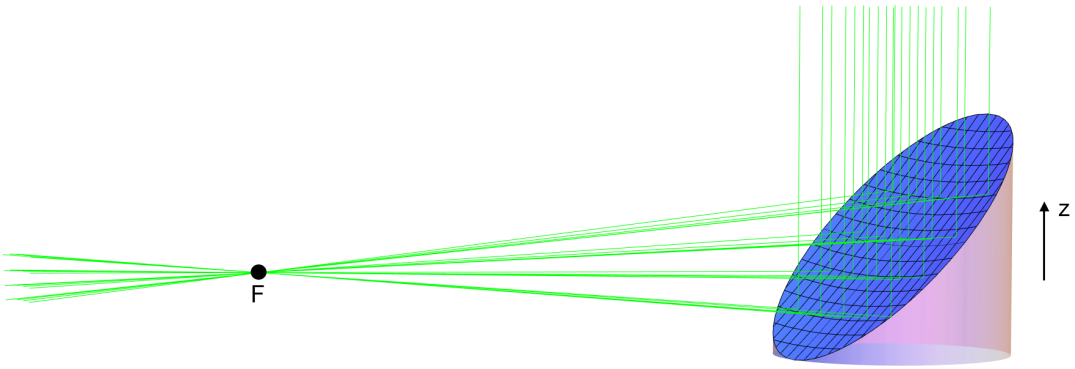

Figure A.2.: An off-axis parabolic mirror focusing collimated light.

now like to know what the polarization of the reflected light is when viewed from the sample, i.e. the point **F**. To extend the model to include the polarization, we look at a collinear bundle of incoming rays with the polarization $\mathbf{E}_{\text{in}}$, obeying the relation $\mathbf{E}_{\text{in}} \cdot \mathbf{k}_{\text{in}} = 0$. One has to keep in mind that s- and p-components of the electric field are reflected differently from the mirror surface: The direction of the s-polarization stays constant on reflection, whereas the direction of the p-component is changed[33]. We thus decompose the polarization of each

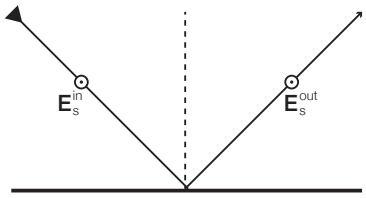

(a) The s-component of the polarization does not change direction on reflection.

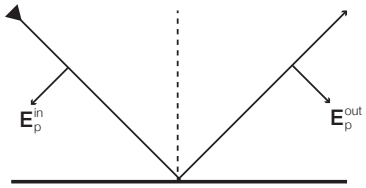

(b) Behavior of the p-component of the electric field on reflection.

Figure A.3.: Difference between s- and p-reflection.

ray into a local s- and p-component, depending on the orientation of the surface normal $\hat{\mathbf{n}}$

[1] To get the parabola surface as it appears for our particular mirror (compare to the datasheet in figure A.1b), we can use the function $z(x, y) = (x^2 + y^2)/12$ in the region $(x - 6)^2 + y^2 \leq 1$.

and the propagation vector $\mathbf{k}_{\text{in}}$:

$$\hat{\mathbf{s}}_{\text{in}} = \mathbf{k}_{\text{in}} \times \mathbf{k}_{\text{out}}, \qquad \hat{\mathbf{s}}_{\text{out}} = \hat{\mathbf{s}}_{\text{in}} \tag{A.2}$$

$$\hat{\mathbf{p}}_{\text{in}} = \mathbf{k}_{\text{in}} \times \hat{\mathbf{s}}_{\text{in}}, \qquad \hat{\mathbf{p}}_{\text{out}} = \mathbf{k}_{\text{out}} \times \hat{\mathbf{s}}_{\text{out}} \tag{A.3}$$

$$\curvearrowright E_{\text{p}} = \hat{\mathbf{p}}_{\text{in}} \cdot \mathbf{E}_{\text{in}}, \qquad E_{\text{s}} = \hat{\mathbf{s}}_{\text{in}} \cdot \mathbf{E}_{\text{in}} \tag{A.4}$$

At this point, we have the polarization in terms of the local coordinates E_{p} and E_{s}. If needed, one can now include a reflectivity dependence: For metals like aluminum, there is usually a few percent deviation between r_{s} and r_{p}. In this calculation, we will assume $r_{\text{p}} = r_{\text{s}} = 1$.
This can also be written in terms of a matrix multiplication[34]:

$$\begin{pmatrix} E_{\text{p}} \\ E_{\text{s}} \\ 0 \end{pmatrix} = \begin{pmatrix} \hat{p}^{\text{x}}_{\text{in}} & \hat{p}^{\text{y}}_{\text{in}} & \hat{p}^{\text{z}}_{\text{in}} \\ \hat{s}^{\text{x}}_{\text{in}} & \hat{s}^{\text{y}}_{\text{in}} & \hat{s}^{\text{z}}_{\text{in}} \\ k^{\text{x}}_{\text{in}} & k^{\text{y}}_{\text{in}} & k^{\text{z}}_{\text{in}} \end{pmatrix} \cdot \begin{pmatrix} E^{\text{x}}_{\text{in}} \\ E^{\text{y}}_{\text{in}} \\ E^{\text{z}}_{\text{in}} \end{pmatrix} \tag{A.5}$$

To finish the analysis, we have to transform the polarization components from the local coordinates back to an expression in terms of $\hat{\mathbf{e}}_x$, $\hat{\mathbf{e}}_y$ and $\hat{\mathbf{e}}_z$. For this, we multiply the vector $(\,E_{\text{p}}\ E_{\text{s}}\ 0\,)^{\intercal}$ with the transposed shape of the matrix used in equation A.5, with the incoming vectors now replaced by the outgoing ones:

$$\begin{pmatrix} E^{\text{x}}_{\text{out}} \\ E^{\text{y}}_{\text{out}} \\ E^{\text{z}}_{\text{out}} \end{pmatrix} = \begin{pmatrix} \hat{p}^{\text{x}}_{\text{out}} & \hat{s}^{\text{x}}_{\text{out}} & k^{\text{x}}_{\text{out}} \\ \hat{p}^{\text{y}}_{\text{out}} & \hat{s}^{\text{y}}_{\text{out}} & k^{\text{y}}_{\text{out}} \\ \hat{p}^{\text{z}}_{\text{out}} & \hat{s}^{\text{z}}_{\text{out}} & k^{\text{z}}_{\text{out}} \end{pmatrix} \cdot \begin{pmatrix} E_{\text{p}} \\ E_{\text{s}} \\ 0 \end{pmatrix} \tag{A.6}$$

In figure A.4, the calculation has been performed for light that is s-polarized with respect to the mirror center. The deviation of the polarization rotation is color-coded. In the neutral area in the middle, the reflected polarization corresponds to the original linear polarization. If one goes further outward, the direction of the polarization is rotated. This makes off-axis parabolic mirrors unsuitable for applications where the polarization of the light has to be preserved.

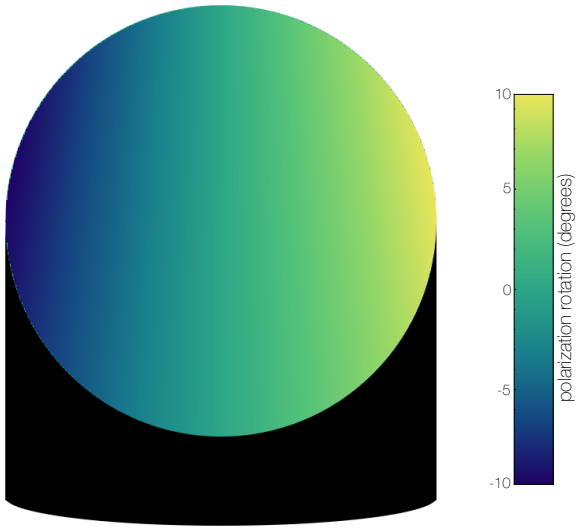

Figure A.4.: Polarization rotation induced by a parabolic mirror, as seen from the focal point **F**.

A.2. Bessel Function Identities

The identities

$$\cos(\delta_0 \sin(\omega t)) = J_0(\delta_0) + 2\sum_{n=1}^{\infty} J_{2n}(\delta_0)\cos(2n\omega t) \tag{A.7}$$

$$\sin(\delta_0 \sin(\omega t)) = 2\sum_{n=0}^{\infty} J_{2n+1}(\delta_0)\sin((2n+1)\omega t) \tag{A.8}$$

can be proven with the generating function of the Bessel functions. The derivation of this generating function is not given here. It can be found, along with the full proof, in [35].

$$e^{\frac{x}{2}(z-z^{-1})} = \sum_{n=-\infty}^{\infty} J_n(x)z^n \tag{A.9}$$

We write $z = e^{i\phi}$ and $i \sin\phi = \frac{1}{2}(e^{i\phi} - e^{-i\phi}) = \frac{1}{2}(z - \frac{1}{z})$. Thus we can rewrite the generating function:

$$e^{\frac{x}{2}(z-z^{-1})} = e^{ix\sin\phi} = \cos(x\sin\phi) + i\sin(x\sin\phi) = \sum_{n=-\infty}^{\infty} J_n(x)e^{in\phi}$$
$$= \sum_{n=-\infty}^{\infty} J_n(x)(\cos n\phi + i\sin n\phi) \tag{A.10}$$

Then, splitting up real and complex parts and using the fact that Bessel functions of odd (even) order are odd (even) functions, we get:

$$\cos(x\sin\phi) = \cancel{\sum_{\substack{n=-\infty \\ n \text{ odd}}}^{\infty} J_n(x)\cos n\phi} + \sum_{\substack{n=-\infty \\ n \text{ even}}}^{\infty} J_n(x)\cos n\phi$$
$$= J_0(x) + 2\sum_{n=1}^{\infty} J_{2n}(x)\cos 2n\phi, \tag{A.11}$$
$$\sin(x\sin\phi) = \sum_{\substack{n=-\infty \\ n \text{ odd}}}^{\infty} J_n(x)\sin n\phi + \cancel{\sum_{\substack{n=-\infty \\ n \text{ even}}}^{\infty} J_n(x)\sin n\phi}$$
$$= 2\sum_{n=0}^{\infty} J_{2n+1}(x)\sin(2n+1)\phi \quad \square \tag{A.12}$$

Table A.1.: Some Jones vectors and matrices used in the thesis. For more elements, see e.g. [6].

polarization state	Jones vector
horizontal linear	$\begin{pmatrix}1\\0\end{pmatrix}$
vertical linear	$\begin{pmatrix}0\\1\end{pmatrix}$
+45° linear	$\frac{1}{\sqrt{2}}\begin{pmatrix}1\\1\end{pmatrix}$
general linear (angle α to x axis)	$\begin{pmatrix}\cos\alpha\\\sin\alpha\end{pmatrix}$
right circular	$\frac{1}{\sqrt{2}}\begin{pmatrix}1\\-i\end{pmatrix}$
left circular	$\frac{1}{\sqrt{2}}\begin{pmatrix}1\\i\end{pmatrix}$

optical element	Jones matrix
general linear polarizer (angle α to x axis)	$\begin{pmatrix}\cos^2\alpha & \cos\alpha\sin\alpha\\\sin\alpha\cos\alpha & \sin^2\alpha\end{pmatrix}$
quarter wave plate	$e^{-i\frac{\pi}{4}}\begin{pmatrix}1 & 0\\0 & i\end{pmatrix}$
phase retarder	$\begin{pmatrix}e^{i\phi_x} & 0\\0 & e^{-i\phi_y}\end{pmatrix}$

A.3. Ellipsometry

Preliminary ellipsometry results in figure A.5 have been obtained by I. Vergara. The measurement was done at room temperature, low temperature results were not yet available during the writing of this thesis.

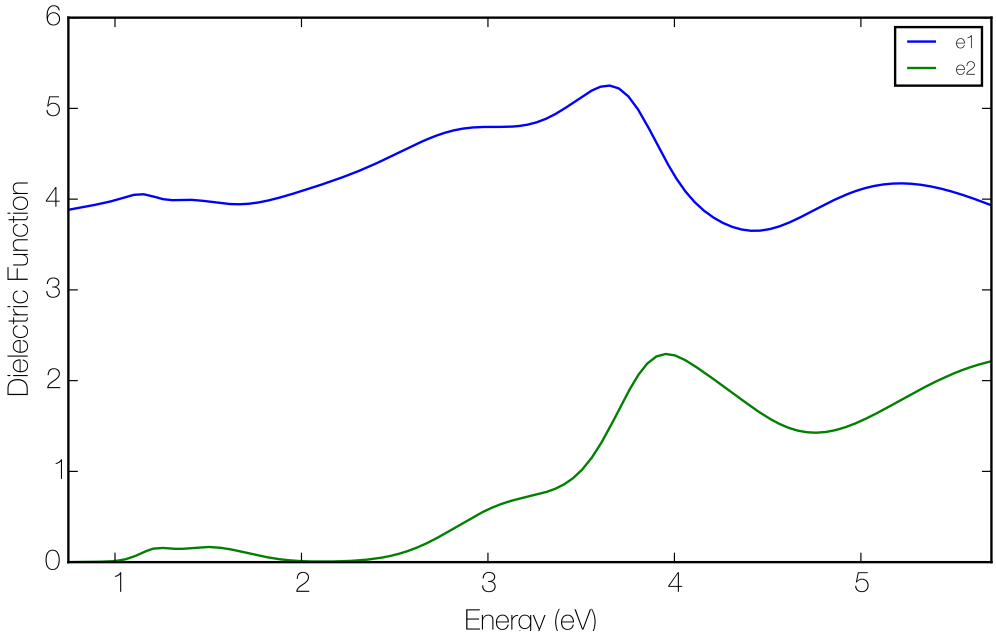

Figure A.5.: Preliminary ellipsometry data of Cu_2OSeO_3 taken by I. Vergara.

A.4. Measurement Software

The measurement software for the polarization spectrometer has been implemented in LabVIEW. Two programs were made:
The first one takes polarization spectra over a wavelength interval with a selectable step size (see figure A.6). Once the parameters (start wavelength, end wavelength, step size, lock-in amplification settings) are put in, the measurement is automatic: The PEM and the monochromator wavelength settings are changed in unison, the filter wheel is rotated to the value appropriate for the current wavelength. Magnitudes and phases of the two lock-ins are collected at the dc/chopped frequency and the PEM first and second harmonics. Changes in temperature are tracked, the rotation and ellipticity values are divided internally. The output file then contains one row for each wavelength step measured.
The second program (see figure A.7) records the polarization state for a single wavelength

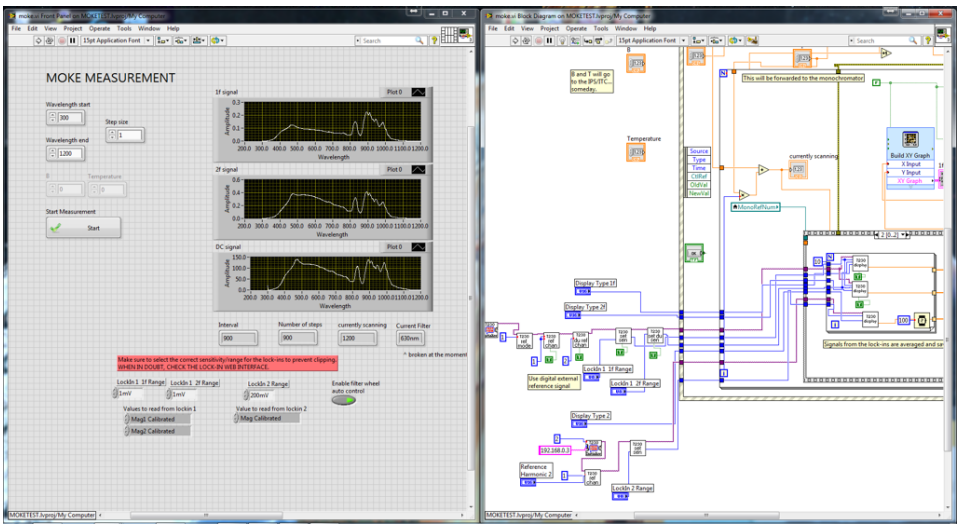

Figure A.6.: Screenshot of the software used to record MOKE spectra. Once the parameters are put in, the measurement is fully automatic.

in time and can be used to track a magnetic field sweep or the behavior over a temperature range. Once the program is set to a certain wavelength, it continuously collects data (magnitudes, phases, temperature, magnetic field) several times a second. The magnetic field or temperature sweep can be controlled with the interface depicted in figure A.8.

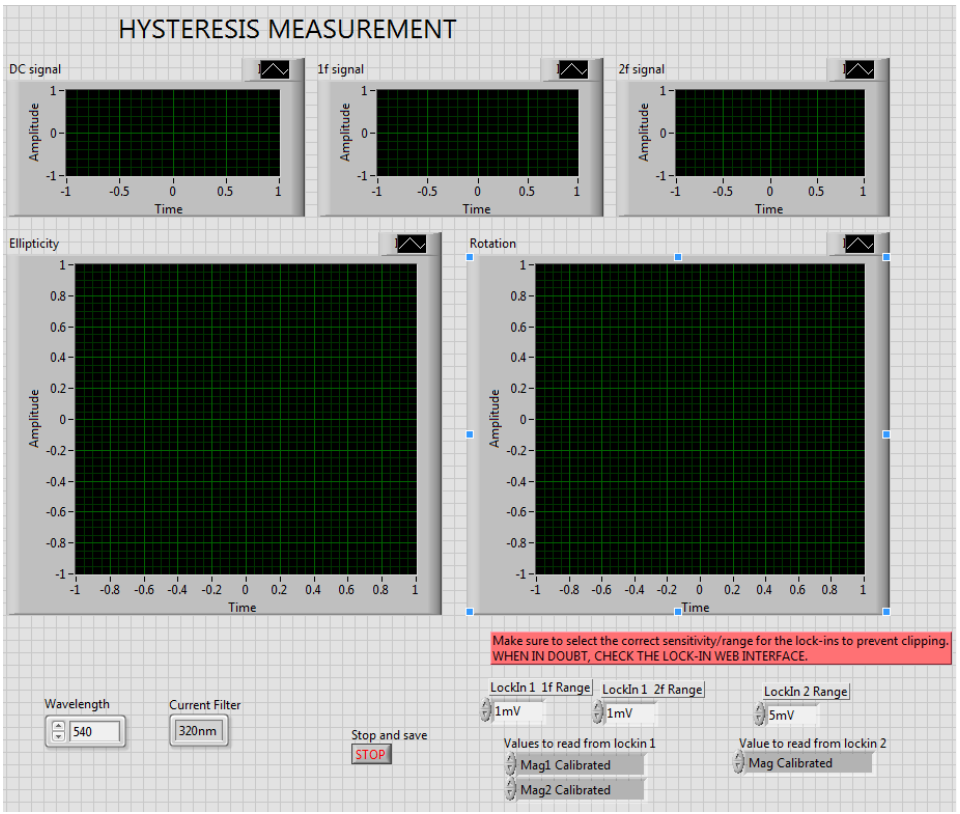

Figure A.7.: Screenshot of the software used to record magnetic field sweeps. All values are continuously recorded until the measurement is stopped.

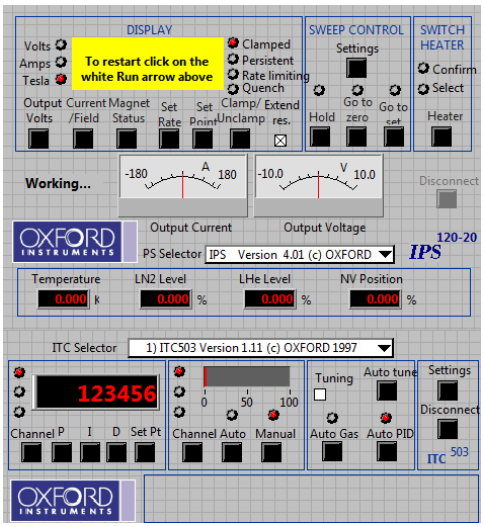

Figure A.8.: Screenshot of the control panel for the Oxford cryostat and magnet. The temperature controller can either be controlled by hand or hold a set temperature automatically. The magnet supports sweeps with customizable sweep rates.

List of Figures

Bibliography

[1] R. Prasankumar and A Taylor, *Optical techniques for solid-state materials characterization* (CRC Press, 2011).

[2] A Zvezdin and V Kotov, *Modern magnetooptics and magnetooptical materials*, Condensed Matter Physics (Taylor & Francis, 1997).

[3] L. Plumer, J. van Ek, and D. Weller, *The physics of ultra-high-density magnetic recording*, Results and Problems in Cell Differentiation (Springer Berlin Heidelberg, 2001).

[4] T. Adams, a. Chacon, M. Wagner, a. Bauer, G. Brandl, B. Pedersen, H. Berger, P. Lemmens, and C. Pfleiderer, "Long-wavelength helimagnetic order and skyrmion lattice phase in Cu 2OSeO 3", Physical Review Letters **108**, 3–8 (2012).

[5] U. of Reading PPLATO, *Light – a wave phenomenon*, [Online; accessed 20-Feb-2015], http://www.met.reading.ac.uk/pplato2/h-flap/phys6_1.html.

[6] F. J. Pedrotti and L. S. Pedrotti, *Introduction to optics* (Prentice Hall, 1993).

[7] Wikipedia, *Circular polarization — wikipedia, the free encyclopedia*, [Online; accessed 20-February-2015], http://en.wikipedia.org/w/index.php?title=Circular_polarization.

[8] F. P. Mena, *Kerr spectroscopy in YVO_3*, Master Thesis, 2000.

[9] P. N. Argyres, "Theory of the Faraday and Kerr effects in ferromagnetics", Physical Review **97**, 334–345 (1955).

[10] P. H. M. van Loosdrecht, *Photons and matter*, University Lecture, 2014.

[11] A. Fox, *Optical properties of solids*, Oxford master series in condensed matter physics (Oxford University Press, 2001).

[12] P. Oppeneer, "Magneto-optical Kerr spectra", Handbook of Magnetic Materials, 229–422 (2001).

[13] K. Sato, "Measurement of magneto-optical Kerr effect using piezo-birefrigent modulator", Jpn. J. Appl. Phys. **20**, 2403–2409 (1981).

[14] S. Polisetty, J. Scheffler, S. Sahoo, Y. Wang, T. Mukherjee, X. He, and C. Binek, "Optimization of magneto-optical Kerr setup: Analyzing experimental assemblies using Jones matrix formalism", Review of Scientific Instruments **79** (2008).

[15]J.-W. G. Bos, C. V. Colin, and T. T. M. Palstra, "Magnetoelectric coupling in the cubic ferrimagnet Cu_2OSeO_3", Phys. Rev. B **78**, 094416 (2008).

[16]S. Seki, X. Z. Yu, S. Ishiwata, and Y. Tokura, "Observation of Skyrmions in a Multiferroic Material", Science **336**, 198–201 (2012).

[17]O. Janson, I. Rousochatzakis, A. Tsirlin, M. Belesi, A. A. Leonov, U. K. Rössler, J. V. D. Brink, and H. Rosner, "The quantum origins of skyrmions and half-skyrmions in Cu_2OSeO_3", Nature Communications **5**, 1–5 (2014).

[18]J. Romhányi, J. V. D. Brink, and I. Rousochatzakis, "Entangled tetrahedron ground state and excitations of the magneto-electric skyrmion material Cu_2OSeO_3", 4 (2014).

[19]M. Belesi, I. Rousochatzakis, H. C. Wu, H. Berger, I. V. Shvets, F. Mila, and J. P. Ansermet, "Ferrimagnetism of the magnetoelectric compound Cu_2OSeO_3 probed by 77Se NMR", Physical Review B - Condensed Matter and Materials Physics **82**, 1–10 (2010).

[20]I. Dzyaloshinsky, "A thermodynamic theory of "weak" ferromagnetism of antiferromagnetics", Journal of Physics and Chemistry of Solids **4**, 241–255 (1958).

[21]K. Everschor, "Current-induced dynamics of chiral magnetic structures", PhD thesis (2012).

[22]C. Schütte, "Skyrmions and Monopoles in Chiral Magnets & Correlated Heterostructures", PhD Thesis (2014).

[23]G. S. Krinchik and V. A. Artemev, "Magnetooptical properties of Ni, Co, and Fe in the ultraviolet, visible, and infrared parts of the spectrum", Sov. Phys. JETP **26**, 1080–1085 (1968).

[24]P. G. van Engen, "An experimental study of the magneto-optical properties of ferromagnetic alloys", PhD thesis (TU Delft, 1983).

[25]O. J. Schumann, "Structural Investigations on Layered Manganites and Ruthenates", PhD thesis (2010).

[26]R. Chartrand, "Numerical Differentiation of Noisy, Nonsmooth Data", ISRN Applied Mathematics **2011**, 1–11 (2011).

[27]J. H. Yang, Z. L. Li, X. Z. Lu, M. H. Whangbo, S. H. Wei, X. G. Gong, and H. J. Xiang, "Strong Dzyaloshinskii-Moriya interaction and origin of ferroelectricity in Cu 2OSeO 3", Physical Review Letters **109**, 1–5 (2012).

[28]L. Jia-Ming, *Photonic Devices* (Cambridge University Press, 2005).

[29]N. Grumman, *Terbium Gallium Garnet - Datasheet*.

[30]T. Schwarze, J. Waizner, M. Garst, A. Bauer, I. Stasinopoulos, H. Berger, C. Pfleiderer, and D Grundler, "Universal helimagnon and Skyrmion excitations in metallic , semiconducting , and insulating chiral magnets", **14** (2013).

[31]Wikipedia, *Chromatic aberration — wikipedia, the free encyclopedia*, [Online; accessed 29-April-2015], (2015) http://en.wikipedia.org/w/index.php?title=Chromatic_aberration&oldid=649864116.

[32]Thorlabs, *Off-axis parabolic mirror mpd269-f01, datasheet*, [Online; accessed 29-April-2015], (2015) http://www.thorlabs.de/thorcat/TTN/MPD269-F01-AutoCADPDF.pdf.

[33]D. Suter and G. S. Uhrig, *Physik III - Optik*, University Lecture, 2011.

[34]G. Yun, S. C. McClain, and R. a. Chipman, "Three-dimensional polarization ray-tracing calculus I", Applied optics **50**, 2866–2874 (2011).

[35]M. Kreh, "Bessel Functions", 1–21 (2012).

Abstract

During the course of this thesis, a polarization spectrometer was built. It is capable of high-resolution measurements of magneto-optical effects, such as the magneto-optical Kerr (MOKE) and Faraday effects. The measurement process has been mostly automated with custom-made software. A mathematical treatment of the measurement method and its limitations is given. After testing and optimization of the setup, measurements were performed on the magneto-electric insulator Cu_2OSeO_3 which hosts a skyrmion phase. With the magneto-optical measurements, it is possible to create a magnetic phase diagram of the compound, which replicates results gathered in neutron scattering experiments with an all-optical technique. Cu_2OSeO_3 is shown to have a very large Verdet constant in a small transmission region in the optical range and possible implications of this are discussed.

B. Acknowledgements and Declaration

Acknowledgment

I would like to thank Prof. van Loosdrecht for the supervision of this thesis and the many fruitful discussions during the last months. Thanks go to Ignacio Vergara for carrying out ellipsometry measurements on the compound. Rolf Versteeg has been a tremendous help and played a very large part in the construction of the lab and the subsequent data analysis. Also, his music selection gave the lab a sense of undeniable swag.
It has been a great learning experience and I would like to thank the whole group for making my time here so enjoyable. Also, I would like to apologize to all friends who I have neglected during the writing of this thesis.
Dank u wel!

Declaration

I hereby declare that I wrote my thesis "Construction of a Polarization Spectrometer and Observation of the Skyrmion Phase in the Magneto-Electric Insulator Cu_2OSeO_3" without any unlawful aids. I further declare that to the best of my knowledge and belief all external authorships have been correctly cited and marked as such.

——————————

Simon Schäfer, Cologne, May 9, 2015